NASA Technical Paper 3257

March 1993

Static and Aerothermal Tests of a Superalloy Honeycomb Prepackaged Thermal Protection System

Mark P. Gorton,
John L. Shideler,
and Granville L. Webb

NASA

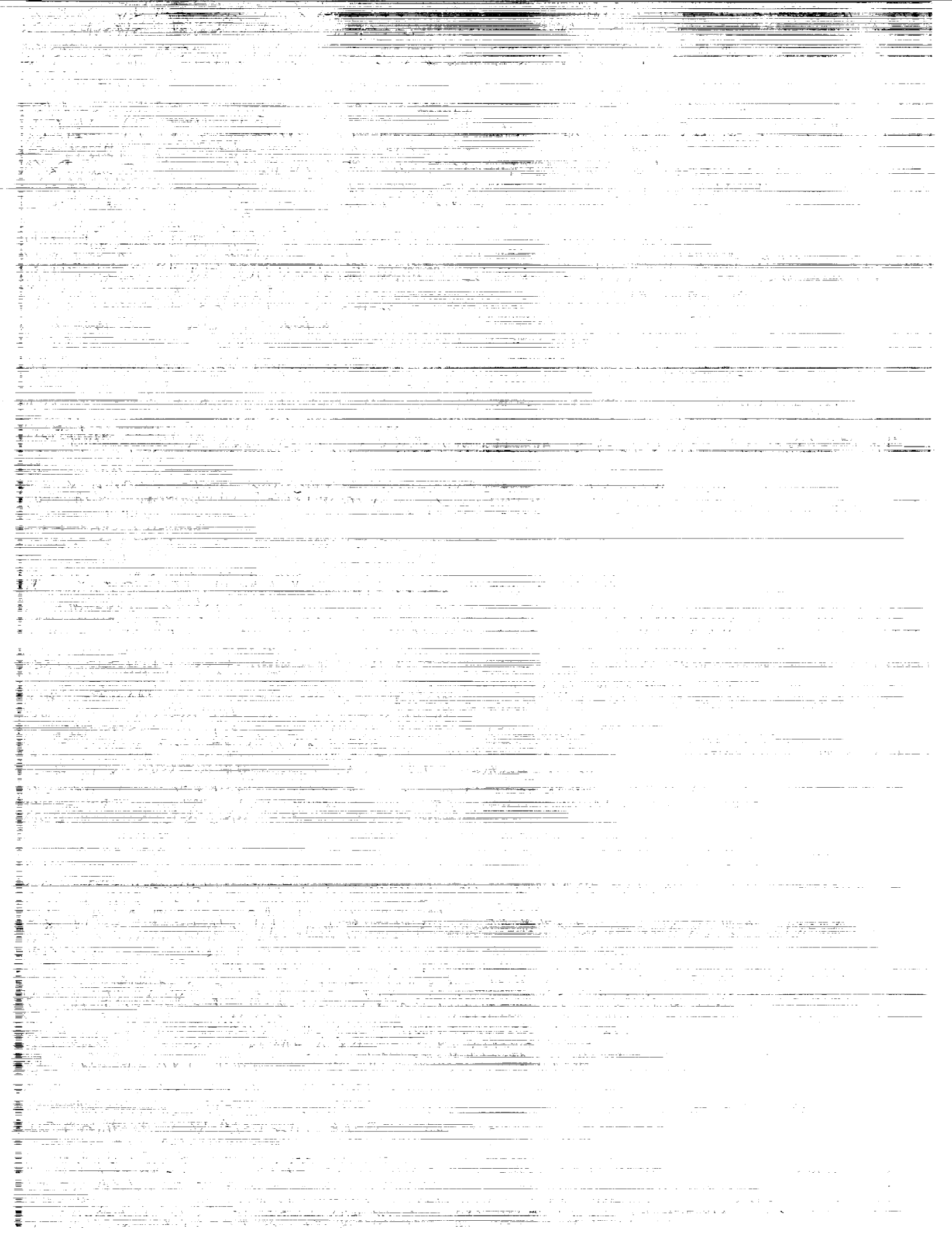

NASA Technical Paper 3257

1993

Static and Aerothermal Tests of a Superalloy Honeycomb Prepackaged Thermal Protection System

Mark P. Gorton
Lockheed Engineering & Sciences Company
Hampton, Virginia

John L. Shideler and Granville L. Webb
Langley Research Center
Hampton, Virginia

National Aeronautics and Space Administration

Office of Management

Scientific and Technical Information Program

The use of trademarks or names of manufacturers in this report is for accurate reporting and does not constitute an official endorsement, either expressed or implied, of such products or manufacturers by the National Aeronautics and Space Administration.

Summary

A reusable metallic thermal protection system (TPS), called superalloy honeycomb prepackaged TPS, has been developed for vehicles with maximum surface temperatures of up to 2000°F. An array of two 12- by 12-in. panels was subjected to radiant heating tests that simulated entry temperature and pressure histories for the Space Shuttle. Results indicate that this thermal protection system, with a mass of 2.201 lbm/ft^2, can successfully prevent the typical aluminum primary structure of an entry vehicle like the Space Shuttle from exceeding temperatures greater than 350°F at a location on the vehicle where the maximum surface temperature is 1900°F. A comparison of measured temperatures with temperatures calculated with a finite-element analysis shows that the maximum measured temperature of the aluminum support plate (304°F) agrees with the maximum calculated temperature (312°F). Acoustic tests performed on the two-panel array caused no settling of the fiberous insulation contained within the panels and caused no change in thermal performance. A flat array of 20 panels was exposed to aerothermal flow conditions at a Mach number of 6.75. The panels were installed in a worst-case orientation with the gaps between the panels parallel to the flow. Results from the aerothermal tests indicated that convective heating occurred from hot gas flow in the gaps between the panels. Proposed design changes to prevent gap heating include orienting panels so that gaps are not parallel to the flow and using a packaged, compressible *gap-filler* material between panels to block hot gas flow in the gaps.

Results from these thermal, acoustic, and aerothermal tests show that the superalloy honeycomb TPS panels can repeatedly endure a realistic entry environment and maintain their effectiveness. The panels limit the primary-structure temperature, have low mass, and exhibit tolerance to damage in an aerothermal environment. Based on these tests, this thermal protection system appears to be a viable candidate for use on future hypersonic vehicles like the Space Shuttle.

Introduction

Space transportation vehicles entering the Earth's atmosphere at hypersonic speeds encounter aerodynamic heating. Some form of thermal protection is usually required to limit the maximum temperature of the primary structure of the vehicle during entry. Ideally, the thermal protection system (TPS) should be reusable and have low mass, long life, and sufficient strength and stiffness to support aerodynamic and thermal loads. Also, the TPS must be able to (1) withstand handling during installation, inspection, and removal, (2) endure less-than-excellent weather conditions during flight, and (3) remain operational after sustaining partial damage.

Three general reusable TPS classes have been developed over the past years: metallic (for temperatures less than about 2300°F, refs. 1 and 2), ceramic (for temperatures less than about 2700°F, ref. 3), and high-temperature composite (for temperatures greater than about 2700°F, ref. 4). Three metallic TPS concepts have been developed and tested for potential application in the lower temperature range: metallic stand-off TPS (ref. 1), multiwall TPS (ref. 1), and superalloy honeycomb (SAHC) TPS (ref. 5). The superalloy honeycomb TPS consists of 12- by 12-in. honeycomb-stiffened panels that encapsulate fiberous insulation. The panels are mechanically attached to the exterior of the primary structure of the vehicle, where they form a reusable and durable insulating layer. The panels are designed for a maximum surface temperature of 2000°F, and depending on the heating history of the design, they can be several inches thick. This report describes the fabrication and testing of a 2-panel array and a 20-panel array of the superalloy honeycomb TPS.

An array of two panels was subjected to radiant heating tests at NASA Johnson Space Center (JSC). The test conditions simulated entry temperature and pressure histories for the Space Shuttle. The two-panel array was also placed in an acoustic chamber at JSC and subjected to an acoustic environment representative of that which occurs near the aft end of the Space Shuttle during liftoff. In addition, the SAHC two-panel array was thermally analyzed with the finite-element method. An array of 20 panels was exposed to Mach 6.75 flow conditions in the Langley 8-Foot High-Temperature Tunnel (8′HTT). The aerothermal tests were performed to study panel behavior in hypersonic flow conditions and to assess the effects of convective heating, particularly in the gaps between panels. Thermal and acoustic test data for the two-panel array were contributed by Donald J. Tillian and James D. Johnston of NASA Johnson Space Center, Houston, Texas.

Superalloy Honeycomb TPS Design and Fabrication

Design Requirements

The superalloy honeycomb TPS panels tested in this program were sized to limit the temperature of the primary aluminum structure of an entry vehicle like the Space Shuttle to less than 350°F. Figure 1 illustrates the typical entry pressure and surface

temperature conditions for which the panels were designed. The pressure and temperature histories represent conditions at Space Shuttle body point 1300 during trajectory 14414.1C (ref. 1). A typical entry cycle lasts about 2000 sec. The maximum entry temperature of 1900°F occurs at about 500 sec into the trajectory at a pressure of 0.26 psia. The surface heating is essentially completed before the pressure starts to rise at about 1600 sec.

A typical SAHC TPS panel, shown in figure 2(a), was designed to support an ascent pressure load of 2 psi and to withstand temperature-gradient-induced thermal stresses associated with the entry temperature history. The panel consists of inner and outer layers of metallic honeycomb-core sandwich with fiberous insulation contained between the two layers. (See ref. 5.) Beaded side closures around the perimeter of the panel join the two layers of honeycomb-core sandwich and enclose the insulation to form a discrete panel. The outer honeycomb-core sandwich, which must survive temperatures up to 2000°F, is made of Inco Alloys Inconel 617. The inner honeycomb-core sandwich, which does not get as hot, is made of lighter weight titanium alloy. Similarly, the outer layer of fiberous insulation, Manville Cerachrome, is a high-temperature insulation (maximum temperature of 2600°F) and is relatively heavy (6 lb/ft^3 density). The inner layer, Manville Q-Fiber felt, is a lower temperature insulation (maximum temperature of 1800°F) and is lighter weight (3.5 lb/ft^3 density) than the outer layer. Overhanging lips on two edges of the panel inhibit flow of hot gases between panels. Underhanging lips on the other two edges protect the material beneath the panels from direct radiation heating. Four mechanical attachments, which are subsequently described in detail, are provided to secure the panel to the primary structure of the vehicle. A vent hole with a 0.31-in. diameter was located in the inner honeycomb-core sandwich of each panel to equalize pressure differentials between the panel interior and exterior. The vent hole was covered with a 400-mesh screen to prevent the entrance of liquid water into the panel.

Panel Fabrication

Each panel was fabricated in a three-step process. In the first fabrication step, an Inconel 617 outer honeycomb-core sandwich and a beaded side-closure assembly were diffusion brazed. The 0.25-in-wide square-cell honeycomb core was fabricated from 0.002-in-thick corrugated foil. The thickness of the face sheets was 0.005 in., and the depth of the core was 0.28 in. The four side closures were beaded by using a forming tool to press corrugations and flanges into 0.003-in-thick Inconel 617 foil sheets that were then trimmed to their final size. A braze alloy (1.97B-0.02C-13.13Cr-3.4Fe-Ni balance) was applied to one side of each face sheet and to one side of a flange on each side closure. The honeycomb core was placed between the face sheets, and the beaded side closures were resistance spot welded to the face sheets. The assembly was placed on a flat reference surface in a vacuum furnace, and tungsten pellets were placed on the assembly to provide contact pressure for the diffusion brazing process. The furnace was evacuated to 10^{-4} torr and heated to 2150°F. The assembly was held at this temperature for 3 min, cooled to 1900°F, and then held at this temperature for 1 hr.

In the second fabrication step, the inner honeycomb-core sandwich was fabricated from 0.006-in-thick face sheets (Ti-6Al-4V) and a 0.170-in-deep core (Ti-3Al-2.5V). The 0.1875-in-wide square-cell honeycomb core was manufactured from 0.002-in-thick corrugated foil. Flanges on two sides of the Ti-6Al-4V face sheets were shaped with form tools during a superplastic forming (SPF) process. After being cleaned, the edges of the honeycomb core were plated with a Liquid Interface Diffusion (LID)[1] bonding material. The core and face sheets were placed together, inserted into a vacuum furnace, and heated to 1725°F to diffusion bond the core to the face sheets.

In the third fabrication step, the Inconel 617 assembly and the titanium assembly were joined together. The flanges of the assemblies were plated with the LID bonding alloy. The Inconel 617 honeycomb and beaded side-closure assembly was filled with a 0.5-in-thick layer of Cerachrome insulation and a 1.39-in-thick layer of Q-Fiber felt insulation. The titanium honeycomb assembly was placed over the Q-Fiber felt insulation, and the flanges of both assemblies were resistance spot welded together to form a panel. The panel was again placed on a flat reference surface in a vacuum furnace at 10^{-5} torr and heated to 1725°F. The flanges of the two assemblies were thus LID bonded together to form a completed panel. Reference 6 provides a more detailed description of this fabrication procedure. Figure 2(b) shows a fully assembled panel, with overall dimensions of 12 by 12 by 2.35 in.

Panel Attachment

Two mechanical attachment concepts were developed: a bayonet-clip attachment concept (ref. 1) and a through-panel fastener assembly concept (ref. 5).

[1] Proprietary joining process for Rohr Industries, Inc.

Both attachment concepts were designed to allow easy installation and removal of panels, tolerance for minor misalignment of panels, and accommodation of thermal expansion and deflection of panels.

The bayonet-clip attachment concept, illustrated in figure 3(a), consists of three parts: a vehicle clip, a Ti-6Al-4V panel clip, and a Ti-6Al-4V bayonet. Two bayonets are LID bonded to the underside of the front of a panel, and two panel clips are LID bonded to the underside of the rear of a panel. Vehicle clips are attached to the vehicle structure at locations matching the TPS panel layout. The bayonet-clip attachment concept requires that panels be installed in rows. The front of the first panel is anchored by inserting its bayonets into the vehicle clips. The bayonets of a panel immediately behind the first panel are inserted through the vehicle clips and then through the panel clips of the first panel. Successive panels are installed in the same manner until a row is completed. Then, the last panel in a row is fastened to the vehicle structure by another attachment concept (i.e., a pair of through-panel fasteners). To remove a panel or a row of panels, this process is reversed.

Figure 3(b) illustrates the through-panel fastener assembly concept. Four Inconel 617 through-panel fastener assemblies, which are diffusion brazed to the Inconel 617 honeycomb layer, are LID bonded to the titanium honeycomb layer during the last step of the panel fabrication process. Shoulder bolts, inserted at each corner of the panel, are used to attach a panel to the vehicle structure. Three of the four holes in the titanium honeycomb (TiHC) layer are oversized to allow lateral movement (due to thermal growth) of the panel. Removal of an individual panel requires the removal of shoulder bolts from the panel and from adjacent panels. The panel is moved laterally and lifted away from the vehicle structure, so that the underhanging lips clear the undersides of surrounding panels. Thus, the use of through-panel fasteners allows the removal of individual panels with minimal disturbance of adjacent panels.

Two-Panel Array Assembly

A two-panel array was assembled and instrumented for cyclic radiant heating tests. As shown in figure 4, the array consisted of two panels that were mechanically fastened to an aluminum plate with bayonet-clip attachments. A nominal gap spacing of 0.220 in. between the two panels was used to accommodate thermal expansion. The aluminum plate was sized to represent the thermal mass of the vehicle structure of the Space Shuttle at a location where the maximum design surface temperature is 1900°F. Strips of Du Pont Nomex felt used to cushion the panels were bonded to the 0.190-in-thick aluminum plate with an elastomeric General Electric RTV (room temperature vulcanizing) silicone adhesive. The felt strips, made of a mat of randomly oriented horizontal Nomex fibers, were 1.0 in. wide by 0.190 in. thick (ref. 7). The strips were laid in a square pattern not only to cushion the edges of each panel but also to minimize air flow beneath each panel. A single gap width of 0.125 in. in the felt pattern under each panel was used to vent the underside of a panel to the atmosphere.

Each of the two panels in the array is about 12 in. wide by 12 in. long by 2.35 in. thick. A diagram of the array (fig. 5) identifies the locations of 26 Chromel-Alumel (type K) thermocouples used to sense panel and aluminum plate temperatures during testing. Five thermocouples were peened to the aluminum plate, nine thermocouples were tack welded to the underside of the panels, three thermocouples were tack welded to panel 1 on the exterior of the side closure in the gap region, and nine thermocouples were tack welded to the upper surfaces of the panels. All thermocouple wires were No. 30 AWG (American Wire Gauge) and were fiberglass sheathed except for the upper surface wires, which were metal sheathed.

After the array was assembled and instrumented, a noncatalytic ceramic coating was applied to the upper surface of the array and allowed to air dry. The 0.0015- to 0.002-in-thick coating is a commercially available, water-based, silica-alumina proprietary coating designated CRC-SBE, which is produced by the Ceramic-Refractory Corporation. It has good adhesion to the Inconel 617 foil sheets, an emittance of 0.65, and the capability of withstanding temperatures greater than 1800°F (ref. 8). The ceramic coating was applied to the surface of the panels with conventional spray painting equipment and air dried at room temperature. The panels were coated to evaluate the adherence of a nonmetallic, noncatalytic coating to an SAHC TPS panel surface. Such a coating is of interest because, for the same entry conditions, a catalytic metallic surface is subjected to a higher heat load than a noncatalytic surface. This difference occurs because metallic surfaces are generally catalytic to the recombination of dissociated air molecules, and the energy released during recombination adds to the heat load. Therefore, a noncatalytic coating increases the thermal efficiency of a metallic TPS by delaying recombination and thus lowering the net heat flux absorbed by the panel. (See ref. 8.)

20-Panel Array Assembly

A 20-panel array was fabricated and instrumented for radiant heating and aerothermal tests. The array, shown in figure 6, was configured to fit a standard panel holder used in the Langley 8′HTT. Two panel sizes, about 12 in. wide by 12 in. long and about 6-in. wide by 12 in. long, were used to fill a 42.5-in-wide by 60-in-long opening in the panel holder. A 0.190-in-thick aluminum plate, representing the vehicle primary structure, supported the panels such that the surfaces of the panels were flush with the surface of the panel holder. The edges of the aluminum plate were sealed to the panel holder with RTV silicone adhesive. A nominal gap spacing of 0.220 in. was used between side closures of adjacent panels. Panels 2A, 2B, 2E, and all panels of row 3 (see fig. 6) were fastened with bayonet-clip attachments; panels 1C and 1D were fastened with through-panel fasteners. The remaining panels were fastened with a combination of bayonet-clip attachments and through-panel fasteners. As with the two-panel array, the panels were cushioned on 1.0-in-wide by 0.190-in-thick Nomex felt strips. The felt strips, which were fitted around the areas having bayonet-clip attachments, were bonded to the aluminum support structure with RTV adhesive.

Figure 7 shows the locations of thermocouple and pressure instrumentation for the 20-panel array. Fifty-five Chromel-Alumel (type K) thermocouples were used to record panel and structure temperatures during testing. The thermocouple mounting methods and sheathing of the No. 30 AWG wire were similar to those used on the two-panel array. For the 20-panel array, 24 thermocouples were mounted on the upper surface of the array, 9 were mounted on the external surfaces of selected side closures (in the gaps between panels), 3 were mounted on the internal surface of a side closure (section D-D of fig. 7), 2 were mounted at the center on the interior face sheets of a panel (section E-E of fig. 7), 10 were mounted on the lower surface of selected panels, and 7 were mounted on the support structure (aluminum plate and frame). The lead wires of the internally mounted thermocouples exited through the bottom of the panel, while the lead wires on the external surfaces of the side closures were routed down the side closure and under the panel. The lead wires of thermocouples mounted on the upper surface of a panel were routed to the trailing edge, down the side closure, and under the panel. Eleven pressure probes were used to monitor pressures beneath the panels and in the gaps between panels. Seven probes, which penetrated the aluminum plate, were located beneath selected panels, and four probes were inserted from the edge of the array into selected gaps. The probes located in the gaps were used to monitor gap pressures to determine whether significant pressure gradients occurred during the aerothermal tests.

The noncatalytic ceramic coating, CRC-SBE, was applied to the upper surfaces of the panels along rows 1 and 2 of the 20-panel array to evaluate its adherence. (This coating was also used on the two-panel array.) Also, a black coating, Pyromark 2500, was applied to the upper surfaces of the panels along rows 3 and 4. Pyromark is a commercially available, high-temperature, high-emittance (0.85) paint, which is manufactured by Big Three Industries.

Test Facilities and Procedures

Cyclic Radiant Heating Tests of Two-Panel Array

The cyclic radiant heating tests were conducted in a radiant heating test chamber at NASA Johnson Space Center. The chamber, shown in figure 8, is designed to simulate the thermal and static pressure environments to which spacecraft thermal protection systems are exposed during the ascent, orbit, and entry phases of a mission.

The test chamber has a volume of 400 ft^3 and can accommodate models up to 2 by 2 ft. A radiant heater and a cryogenically cooled panel located inside the test chamber are mounted on rails to allow either one to be positioned over a test model during testing. (The cryogenically cooled panel was not used during these tests.) The heater consists of electrically heated graphite elements enclosed in a nitrogen-purged fixture box. One side of the fixture box is a heated niobium susceptor plate that reradiates thermal energy to the test model. A mechanical vacuum pump is used to control static pressure conditions within the chamber. Thus, a test model can be heated or cooled while pressure conditions are maintained. For the cyclic radiant heating tests, only the pressure and radiant heater systems were used to simulate entry conditions for the two-panel array.

The test model, shown in figure 9, contained the two-panel array and its support structure. The support structure consisted of an aluminum panel holder and several types of insulation. The insulation was located beneath and around the sides of the array to minimize heat loss between the array and the panel holder during testing.

Heater operating conditions, environmental test conditions, and model temperature response data were recorded by two data acquisition systems. The first system is an analog-to-digital recording system

that digitizes analog data for all channels and records the data on magnetic tape. The second system, which records and displays real-time data from the first system, consists of self-balancing potentiometer strip-chart recorders that also serve as a backup system for the analog-to-digital system.

The array was subjected to an elevated temperature cure cycle for about 4600 sec to remove the volatile components from the ceramic coating. The first step of the cure cycle consisted of heating the surface of the panels, under ambient pressure, from room temperature to 225°F over a period of 1000 sec and holding at this temperature for 900 sec. The second step consisted of increasing the surface temperature to 350°F over a period of 300 sec and holding at this temperature for 900 sec. The third step consisted of increasing the surface temperature to 500°F over a period of 300 sec and holding at this temperature for 900 sec. The fourth step consisted of turning off the heaters at 4300 sec and allowing the surface of the panels to air cool to ambient temperature.

After the cure cycle, the array was subjected to 26 thermal-pressure cycles in the test chamber. A cycle consisted of evacuating the chamber to 10^{-4} torr and exposing the array to the surface temperature and static pressure histories shown in figure 1. The details of the thermal-pressure cycles are summarized in table I. The maximum surface temperature for cycles 1 through 25 was the design temperature of 1900°F. The surface of the array was intentionally exposed to an over-temperature condition of 2000°F during cycle 26, and the array was exposed to acoustic tests between cycles 16 and 17.

Acoustic Tests of Two-Panel Array

The two-panel array was subjected to acoustic tests in the Sonic Fatigue Laboratory (SFL) located at Johnson Space Center. The SFL is used to expose structural components to simulated rocket-launch-induced and aerodynamically induced acoustic noise environments. The primary test equipment consists of a 16- by 20- by 40-ft reverberant test chamber that can accommodate panels up to 15 by 20 ft. Test sound levels to 166 dB (reference level: 2.9×10^{-9} psia) can be imposed on a test article. Excitation is normally provided by one 20-Hz, one 40-Hz, two 100-Hz, and eight 250-Hz horns. The horns are driven by appropriate low- or high-frequency air modulators (noise generators). These noise generators operate by chopping a compressed air stream provided by a manifold. The manifold distributes the air from three compressors that can be operated individually or in combination to provide a continuous total flow of 54 000 standard ft^3/min (SCFM) at a pressure of about 30 psig. As many as twenty 300 000-acoustic-watt and eighteen 10 000-acoustic-watt noise generators are available to drive the horns. The noise generators are controlled by 24 solid-state power amplifiers, each having an output capability of 4 kVA.

The acoustic test assembly was located on the floor of the sound chamber and instrumented with microphones and accelerometers. (See schematic shown in fig. 10.) The two-panel array was placed on a 0.25-in-thick foam pad, and the sides of the array were shielded from the sound chamber environment by a plastic sheet and a layer of putty. The sheet was placed between the putty and the sides of the panels to protect the panels from putty contamination. Four microphones were mounted on the floor of the chamber, each located about 6 in. from a corner of the array. Two accelerometers, each with a mass of 1.919×10^{-4} slugs (2.8 g), were mounted on the surface of panel 1. (See fig. 10.) Accelerometer A1 was located 2 in. from a corner of the panel, and accelerometer A2 was located at the center of the panel.

After being exposed to the 16 thermal cycles described in table I, the array was exposed to the acoustic spectrum (fig. 11) that corresponds to an overall sound pressure level of 161 dB. The spectrum is representative of the sound environment near the aft end of the Space Shuttle during launch. The array was exposed to the acoustic spectrum for 15 min. Based on the assumption that the most severe acoustical exposure occurs during the first 8 sec. of launch (ref. 2), this exposure approximates the cumulative acoustic environment for 25 missions with a scatter factor of 4.

Aerothermal Tests of 20-Panel Array

The 20-panel array was exposed to thermal and aerodynamic loads at hypersonic speeds in the Langley 8′HTT. The tunnel is a large blowdown facility that can generate, for run times up to about 2 min, a test stream that simulates conditions at a nominal Mach number of 7 at altitudes between 80 000 and 125 000 ft. (See schematic shown in fig. 12.) The high energy needed for this simulation is obtained by burning a mixture of methane and air under pressure in the combustor (fig. 12(a)) and expanding the products of combustion through a conically contoured nozzle into an open-jet test chamber. The flow enters a supersonic diffuser where an air ejector pumps the flow through a mixing tube and exhausts the flow through a subsonic diffuser into the atmosphere. This tunnel operates at combustor total temperatures between 2060°F and 3140°F, at free-stream dynamic pressures from 2.0 to 12.5 psia,

and at free-stream unit Reynolds numbers per foot from 3.0×10^5 to 3.0×10^6.

A radiant heating system, located beneath the test chamber, was used to preheat the array before its insertion into the hypersonic test stream and to protect the array from adverse tunnel start-up transients and acoustic loads. The heater system consisted of quartz-lamp radiators powered by an Ignitron power supply and controlled by a closed-loop servo system. References 9 and 10 contain more detailed information about the 8′HTT.

The test model consisted of the 20-panel array installed in a panel holder that was attached to a hydraulically actuated elevator located beneath the test chamber of the 8′HTT. Before tunnel start-up, the test model was positioned in a pod below the test chamber and was covered with quartz-lamp radiators (fig. 12(b)). After the model was preheated and the desired flow conditions were established, the radiant heaters were retracted and the model was rapidly inserted into the hypersonic test stream (fig. 12(c)). A pitch system located on the elevator positioned the model at an angle of attack of 16° during the insertion process. These combined preheating and aerothermal tests required close coordination of the two test modes. When operational problems prevented the tunnel from starting, the test was aborted and a radiant preheating test was performed.

Table II summarizes the details of the coating cure, radiant heating, radiant preheating, and aerothermal test conditions. The 2 high-temperature coatings applied to the surface of the 20-panel array were cured with a procedure similar to the one used to cure the coating on the 2-panel array. The cure process was divided into four separate cycles to avoid overheating the test model; three cycles were used to cure the ceramic coating, and one cycle was used to cure the black coating. Test 3 consisted of heating the surface of the panels from ambient temperature to 225°F over a period of 1000 sec, holding at this temperature for 1000 sec, and then turning the heaters off and allowing the array to cool. Test 4 consisted of heating the panels from ambient temperature to 480°F over a period of 2500 sec and turning off the heaters and allowing the array to cool. Test 5 consisted of heating the surface of the array from ambient temperature to 480°F, holding at this temperature for 2000 sec, and turning the heaters off and allowing the array to cool. Test 6 was used to cure the black coating. This test consisted of heating the surface of the array from ambient temperature to 480°F over a period of 1000 sec and holding at this temperature for 1500 sec, increasing the surface temperature to 1000°F and holding for 100 sec, and then turning the heaters off and allowing the array to cool.

A radiant heating test consisted of exposing the surface of the array to the same temperature profile used in the radiant heating tests for the two-panel array but at atmospheric pressure. Three radiant heating tests (tests 7–9) were conducted to check the heater operation and to determine that the heater and model could withstand 200 sec at maximum panel temperature (the time period allotted for the start-up of the 8′HTT before an aerothermal test). The radiant preheating tests (tests 10, 11, 18, and 19) were radiant heating tests that resulted because scheduled aerothermal tests were aborted.

An aerothermal test was initiated with a radiant preheating of the model surface to a specified maximum surface temperature. The tunnel was started, the lamps were turned off and retracted, and the model was rotated to a desired angle of attack and inserted into the hypersonic flow stream. The model was held in the flow stream for up to 20 sec, after which it was retracted into the pod. The tunnel flow was then stopped and the model was allowed to cool by natural convection. Thus, the total test time was typically 2000 sec, even though a tunnel run was completed within the first 500 sec. The array was exposed to four aerothermal tests (tests 13–15 and 20). Figure 13 shows a typical temperature history of an aerothermal test.

During radiant heating tests and preheating before aerothermal exposure, thermocouple output signals were recorded at 2-sec intervals. During the aerothermal portion of the tests, pressure and temperature data were recorded at 20 samples/sec. Free-stream conditions in the test chamber were determined from reference measurements of the combustion chamber and from results of tunnel-stream survey tests such as those reported in reference 10. Table III summarizes the details of the wind tunnel test conditions for the aerothermal tests.

Figure 14 shows the 20-panel array and panel holder installed in the 8′HTT. A 1.0-in-thick layer of rigid Glasrock ceramic insulation, which surrounded the array, was used to thermally protect the panel holder. A sharp leading edge with a lateral row of 0.190-in-diameter spherical boundary-layer trips was used to promote a uniform turbulent boundary layer (ref. 10). The panels were installed in the panel holder so that two of their edges were parallel to the flow direction. This installation was considered a worst-case orientation for the panels with respect to the flow. Fences attached to each side of the panel holder were used to provide a relatively uniform

two-dimensional flow over the surface of the panel holder. The light-colored coating on the panels on the right in figure 14 is the ceramic, noncatalytic coating, and the dark-colored (black) coating on the panels on the left is the high-temperature, high-emittance paint.

Thermal Analysis

The thermal response of the SAHC two-panel array was predicted with a finite-element computer program called the SPAR Thermal Analyzer (ref. 11). The SPAR program can be applied to steady-state and transient thermal-analysis problems involving conduction, convection, radiation, and mass transport.

Finite-Element Thermal Model

The finite-element thermal model shown in figure 15 represents a section of the array extending from the center of panel 1 to the center of panel 2. The Inconel 617 honeycomb sandwich, Cerachrome insulation, Q-Fiber felt insulation, titanium honeycomb sandwich, Nomex felt, air, and aluminum were represented by three-dimensional (3-D) hexahedral conduction elements. Elements representing air were located between the side closures in the gap region and between the underside of each panel and the aluminum plate. Heat transfer through the air was by conduction. The Inconel 617 metal side closure, overhanging lip, and underhanging lip were represented by two-dimensional (2-D) quadrilateral radiation elements superimposed on 2-D quadrilateral conduction elements. The gap region, treated as an enclosure for radiation analysis purposes, also contained 2-D quadrilateral radiation elements on the front and back openings of the gap. Although three-dimensional elements were used throughout the model, the analysis was considered to be a two-dimensional analysis because heat transfer occurred only in the X-Y plane. Adiabatic wall boundary conditions were applied to the four sides and the bottom surface of the model. Measured surface temperature data from the radiant heating tests (cycle 5) of the two-panel array were used as input data for a time-dependent, temperature boundary condition that was uniformly applied to the top surface of the model. Conduction and radiation were the primary modes of heat transfer considered; convective heat transfer was neglected in the analysis.

The model, consisting of 1146 nodes and 585 elements, represented a region 2.68 in. high, 12 in. long, and 0.10 in. thick. The spacing between the panels was 0.040 in. wide at the top of the gap and 0.232 in. wide at the bottom of the gap. These dimensions account for upper and lower face sheet expansions due to their respective increases in temperature at the time of maximum surface heating. Even though the gap dimensions on the actual array changed throughout the thermal cycle because of thermal deformations, this fixed-gap geometry was used throughout the analysis. Also, a gap width dimension of 0.240 in. at room temperature was used (for analytical purposes only) as the reference spacing between adjacent panels.

Thermophysical Properties

Figure 15 shows materials represented in the finite-element model, and tables IV and V list the thermophysical properties used in the analysis. The thermophysical properties of all the materials are functions of temperature; the properties of the Cerachrome fiberous insulation and the Q-Fiber felt fiberous insulation are functions of temperature and pressure. Static pressure was input to the analysis as a function of time. Values of thermal conductivity were obtained as follows: Inconel 617 metal (ref. 12), titanium (ref. 13), air (ref. 14), and Nomex and aluminum (ref. 15). Inconel 617 honeycomb sandwich, titanium honeycomb sandwich, Cerachrome insulation, and Q-Fiber felt insulation were treated as materials having an effective thermal conductivity. Effective thermal conductivity, sometimes referred to as apparent conductivity or as an overall coefficient of heat transfer (ref. 16), combines the effects of heat transfer by conduction, convection, and radiation into a single conduction term.

Orthotropic values of effective thermal conductivity were required because differences in values of conductivity exist within the insulation because of fiber direction and within the honeycomb core because of core orientation. Values of conductivity in the through-the-thickness (y-) direction for the insulation materials and the honeycomb-core sandwiches were obtained from reference 5. Based on recommendations from the manufacturer, values of conductivity in the in-plane (X-Z plane) direction for the insulation materials were 35-percent higher in the fiber direction (in-plane direction) than in the through-the-thickness direction. The in-plane values for each honeycomb sandwich were calculated by dividing the cross-sectional area of the metal by the total cross-sectional area and then multiplying this ratio by the value of conductivity for the appropriate metal. The conductivity of air within the cells is an order of magnitude less than the conductivity of either metal and was therefore neglected.

Figures 16(a) and 16(b) show the effective thermal conductivities of Q-Fiber felt insulation and of Cerachrome insulation at atmospheric pressure as functions of temperature. The solid and dashed curves shown in figure 16(a) are the upper and lower boundaries of data taken from references 5 and 17 to 19. The data used to generate the curves in figure 16(b) were obtained from references 5, 17, and 20. The data for Q-Fiber felt insulation (fig. 16(a)) show little scatter throughout the temperature range; however, significant scatter exists within the data for Cerachrome insulation (fig. 16(b)), especially at the higher temperatures. An 87-percent difference in conductivity exists between the lower boundary and upper boundary at 2000°F. The values at the lower boundary shown in the figures, which were taken from reference 5, were used as input in the finite-element thermal analysis. Table IV is a listing of the data for the lower boundary presented as a function of temperature and pressure.

The thermophysical properties assigned to the radiation elements were emissivity, reflectivity, and absorptivity. These properties, which are listed in table V, were held constant in temperature. Elements with an emissivity of 1.0 (blackbody elements) were used to close the front and back openings of the gap. These elements simulated radiation exchange between the gap and the portions of the gap outside the plane of the model.

Results and Discussion

Thermal Performance of Two-Panel Array

The two-panel array was subjected to 26 entry thermal-pressure cycles with the temperature and pressure histories shown in figure 1. The first four cycles, which were used to develop consistent operating procedures, yielded test data that showed variations in cycle-to-cycle maximum surface temperatures. Consistent panel surface temperature distributions and consistent maximum surface temperatures occurred from cycle 5 to cycle 25. Figure 17 shows a surface temperature distribution (cycle 5 at $t = 620$ sec) that is representative of cycles 5 through 25. The isotherms in the figure were estimated by linearly interpolating temperatures obtained from the nine surface thermocouples mounted on the array. A nearly uniform temperature distribution existed over the outer surface near the center of the array; however, temperatures near the corners were about 200°F lower than temperatures at the center because of edge effects.

As expected, the temperature distribution through the thickness at the center of a panel differs from the temperature distribution through the thickness at the edge of a panel. The differences occur because the conduction path through the thickness at the center of a panel is predominantly through the insulation, which has low thermal conductivity. The conduction path at the edge of a panel is predominantly through the thin metal foil of the side closure, which has high thermal conductivity. Radiation heating in the gap region also contributes to the heat transfer at the edge of a panel. Figure 18(a) shows the temperature histories measured at the center of panel 1 for cycles 5 and 25. The temperatures were measured on the upper and lower surfaces of the panel (locations A and B) and on the aluminum plate directly beneath the panel center (location C). Figure 18(b) shows similar temperature histories measured at five locations in the gap region. The pair of curves labeled D represents the temperature history of the surface of the panel; likewise, the remaining four pairs of curves represent the temperature histories at locations E, F, G, and H.

The maximum temperature on the bottom of panel 1 near the edge (fig. 18(b), location G) was about 100°F higher than that at the center (fig. 18(a), location B). However, the temperature difference between locations B and G was not large enough to locally affect the temperature response of the aluminum plate because of the relatively high thermal conductivity of aluminum. The similarity of results from cycle 5 and cycle 25 illustrates the consistency of the tests and indicates that no degradation occurred in the thermal performance of the panel.

Results from the finite-element thermal analysis are compared, in fig. 19(a), with temperatures measured during cycle 5 at the center of panel 1. The peak temperature on the surface of the array (location A) occurred at about 500 sec, and the peak temperature on the underside of the panel (location B) occurred at about 1200 sec. The calculated temperatures on the underside of the panel underpredicted the measured temperatures by as much as 80°F during the period of high transient heating from 500 sec to 1500 sec. Throughout the entire entry period, the calculated and measured temperatures of location C on the aluminum plate agreed within 10°F.

Figure 19(b) shows the calculated and measured temperatures in the gap region for cycle 5. The calculated temperatures underpredicted the measured temperatures during the period from 500 to 1500 sec, except at location E, where the maximum measured temperature was overpredicted by about 50°F. Maximum temperatures at locations F, G, and H were underpredicted by 150°F, 250°F, and 75°F, respectively. Throughout the entry period, the calculated

and measured temperatures at location I on the aluminum plate agreed within 20°F. During all 26 entry cycles, the TPS panels repeatedly limited the maximum temperature of the aluminum structure to well below the design limit of 350°F.

Although the reason for the differences between calculated and measured temperatures during transient heating is not known, the use of standard thermal material properties may have caused the differences. These properties are determined from measurements taken during steady-state conditions (refs. 19 and 20) and may not be adequate for the prediction of temperatures under highly transient conditions. Nevertheless, the relatively accurate prediction of the panel, gap region, and aluminum plate temperatures after 1500 sec (less transient condition) indicates that the overall thermal performance of the TPS panels can be predicted.

Parametric Study

The effects of varying several parameters were studied to determine whether discrepancies between predicted and measured gap temperatures resulted from inadequate analytical modeling of the two-panel array. The effects of changes in the finite-element mesh pattern, the values of thermal conductivity, the values for emissivity of the radiation elements facing into the gap, the method of calculating view factors, and the gap geometry were examined. Finally, the placement of thermocouples and thermocouple lead wires in the gap region was examined to determine how temperature measurements are affected.

A 280-degree-of-freedom model of the gap region, which contained the same element mesh pattern as that used to represent the gap region on the larger 1146-degree-of-freedom model, was incrementally refined to 700 degrees of freedom. An increase in maximum temperature at the bottom of the gap of less than 20°F resulted from the mesh refinement; thus, this small increase indicates that the initial mesh pattern was adequate.

As previously noted, values of effective thermal conductivity for Cerachrome and Q-Fiber felt insulation, defined by the lower boundaries in figures 16(a) and 16(b), were used as input in the analysis. Because a wide range of scatter existed in the conductivity data for Cerachrome insulation, the analysis was repeated with values of effective thermal conductivity defined by the upper boundary in the figures. Because of the increased conductivity, better agreement between calculated and measured temperatures was expected. However, the maximum temperatures in the gap region at locations E, F, and G (fig. 19(b)) increased less than 20°F. Thus, the thermal conductivity of the insulation does not appear to be a dominant parameter governing gap region temperatures.

Changes in values of emissivity and view factors for the radiation elements were investigated to determine their effects on gap region temperatures. Values of emissivity were arbitrarily increased from 0.6 (with a reflectivity of 0.4) to an emissivity of 1.0 (with a reflectivity of 0.0). Calculated gap region temperatures changed less than 20°F as a result of the use of these two extreme values of emissivity; thus, the predicted temperatures were relatively insensitive to changes in emissivity. As described previously, view factors were calculated by a procedure that treated the gap region as an enclosure. To verify that the radiation energy distribution within the gap region was accurate, temperatures were calculated by a second procedure that used a set of view factors determined by the cross-string method (ref. 15). The temperatures calculated by the two procedures were essentially the same. Thus, the radiation energy distribution within the gap region was consistent between the two methods.

In addition to calculating view factors, different gap width dimensions were examined to determine how the distance between the panels affects side-closure temperatures. As previously noted, spacings of 0.040 in. at the top of the gap and 0.232 in. at the bottom of the gap were used throughout each transient analysis. The gap width was arbitrarily increased by 0.100 in. The enlarged gap dimension of 0.140 in. at the top and 0.332 in. at the bottom of the gap was considered extreme. Nevertheless, the calculated temperatures at the lower portion of the side closure increased by about 100°F. This temperature increase was significant but not sufficient by itself to attain good agreement between calculated and measured temperatures. Thus, it appears that uncertainties in the gap region geometry do not solely account for the discrepancies between predicted and measured gap temperatures.

Another potential source of error, the measurement of the gap region temperatures, may have been affected by the existence of the thermocouples and thermocouple lead wires attached to the exterior surface of the side closure in the gap region. The thermocouples and thermocouple lead wires may have interfered with the radiation heat transfer characteristics in the gap region and caused temperatures sensed at the thermocouple junctions to be too high. Evidence to support this hypothesis is addressed in a subsequent section. Consequently, the discrepancies between predicted and measured panel and gap region temperatures may have been due not only to

deficiencies in the analysis but also to temperature measurement errors.

Structural and Acoustic Performance of Two-Panel Array

The two-panel array is shown in figure 20. As previously discussed, the array was subjected to a coating cure cycle, radiant heating cycles, and acoustic tests. Before the coating cure cycle, the surface of the array had developed a whitish discoloration. (See fig. 20.) This discoloration resulted from water absorption that occurred during the period between application of the coating and the curing cycle. The whitish discoloration, however, disappeared after exposure to the first radiant heating cycle.

Exposure of the 2-panel array to 26 thermal-pressure cycles caused intracell buckling of the outer Inconel 617 face sheets and buckling of the overhanging lip. (See fig. 21.) The buckles did not impair the thermal or structural performance of the panels. The intracell buckling of the face sheets initially occurred only on some cells during the fabrication of the individual panels. During the 26 thermal-pressure cycles, the intracell buckling pattern gradually changed to a nearly uniform convex pattern. The height of the dimples was about 0.004 to 0.006 in. above the surface of the panel. The overhanging lip on panel 1, which projected over the edge of panel 2, buckled into a wavy pattern as a result of being constrained from thermal expansion by the cooler side closure. The buckled section of the lip was 4.5 in. long and was located midway along the lip. The amplitude of the buckle pattern was about 0.05 in. from crest to valley, and the wavelength was about 1.5 in. from crest to crest. Such surface roughness is not expected to have an effect on the thermal performance of the TPS because it is within the aerodynamic boundary layer over most of the vehicle surface. Blistering of the surface coating occurred during the first and second thermal-pressure cycles, after which no additional blistering was evident. Inadequate cleaning of the thin outer surfaces of the array before application of the noncatalytic coating is believed to be the cause of the blistering. (Several test samples, adequately cleaned before the coating process, were exposed to 80 thermal shock cycles from room temperature to 2000°F without blistering, ref. 8.)

The two-panel array was subjected to acoustic tests between thermal-pressure cycles 16 and 17. However, before the acoustic testing was started, the overhanging lip along the right half of the edge of panel 2 was unintentionally bent down, which caused some local buckling to occur along the bottom edge of the side closure. More importantly, the outer edge of the felt that supported the underside of this side closure was inadvertently installed incorrectly during the initial assembly. The edge of the felt, which by design was to be positioned 0.25 in. beyond the edge of the panel, was positioned 0.125 in. inward from the edge of the panel. At the conclusion of the acoustic tests, several cracks greater than 0.125 in. long were observed along the bottom edge of the incorrectly supported side closure. Figure 22 shows an edge view of the acoustic damage on panel 2. Because no damage occurred on the other seven sides of the two panels that were properly supported by the Nomex felt, the damage shown in figure 22 is attributed to incorrect placement of the Nomex felt and to the handling damage that occurred before the acoustic tests.

The condition of the fiberous insulation contained inside panel 2 was examined after all radiant heating cycles and acoustic tests were completed. Figure 23 shows four layers of insulation: the top layer is Cerachrome insulation, and the three remaining layers are Q-Fiber felt insulation. Both insulation materials appear unchanged from pretest conditions. No settling of either insulation material was observed. Although a definitive assessment of the life of the TPS panels would require further tests, including combined thermal-acoustic tests, overall results from these thermal and acoustic tests show that the panels can endure realistic thermal and acoustic environments and maintain their effectiveness.

Aerothermal Performance of 20-Panel Array

As previously discussed, the 20-panel array was subjected to 20 tests in the 8′HTT to study panel behavior in hypersonic flow conditions and to assess the effects of convective heating, particularly in the gaps between panels. Tables II and III describe the nature of the tests, which included coating cure, radiant heating cycles, and aerothermal exposure. Temperatures were measured on the surface of the panels, beneath the panels, and between the panels. The thermal performance for the 20-panel array is not directly comparable with that for the 2-panel array because of the effects of the higher thermal mass of the panel holder and because the aerothermal preheating and radiant heating cycles occurred under atmospheric pressure, which caused a reduction in thermal efficiency of the fiberous insulation within the panels.

Figures 24(a) and 24(b) show typical temperature histories for two radiant heating cycles (tests 7 and 8). The temperature data were obtained at or near sections A-A, B-B, C-C, and D-D. (See

fig. 7.) All temperatures shown were measured in the gaps between panels except the surface temperatures, which were measured about 6 in. from the corresponding section location. All gap thermocouples and thermocouple lead wires were mounted externally (solid lines in fig. 24) to the panel side closures except those at section D-D, which were mounted internally (dashed lines in fig. 24). Temperatures at the top of each gap were not available because thermocouples mounted at the top of the gaps were damaged in previous tests.

Temperatures sensed by externally mounted thermocouples were, in general, higher than temperatures sensed by internally mounted thermocouples. Although the externally mounted thermocouples were not located at the same position on the array as the internally mounted thermocouples (section D-D), the surface temperatures measured at section D-D were equal to or higher than those at section A-A. A comparison of temperatures at sections D-D and A-A in test 7 and test 8 (fig. 24) shows that externally mounted thermocouples at the middle and at the bottom of the gap sense higher temperatures and sense temperature changes more rapidly than internally mounted thermocouples. These comparisons indicate that the externally mounted thermocouples and thermocouple lead wires, as a result of being in a more exposed location, were sensitive to radiation heat transfer. Additionally, the externally mounted thermocouple lead wires may have prevented the gaps from closing when the panels were heated. These heating effects may have also occurred during the testing of the two-panel array because the two-panel array had similar thermocouple instrumentation and was subjected to similar radiant heating conditions.

Figure 25 shows a typical temperature history for an aerothermal test (test 13). The temperatures shown were measured at section E-E at the center of panel 2C. (See fig. 7.) The inset shows the temperature history with an expanded time scale from 30 sec before the time labeled *model-in* (when the model was inserted into the tunnel flow) to the time labeled *model-out* (when the model was removed from the tunnel flow). Thermocouples 15 and 44 were located on the outer and inner face sheets of the Inconel 617 honeycomb sandwich, thermocouples 45 and 30 were located on the inner and outer face sheets of the titanium honeycomb sandwich, and thermocouple 54 was located on the aluminum plate. The surface of the array was preheated with the radiant heat lamps to about 1900°F. During the time required to retract the heaters and insert the model into the hypersonic flow, the surface temperature of the array decreased to about 1100°. (For example, see thermocouple 15, fig. 25.) When the model was inserted into the flow, the surface temperature of the panel rapidly increased to about 1700°F because of aerodynamic heating. The constant temperature of thermocouple 30 (fig. 25) is representative of all the thermocouples located on the underside of the panels and indicates that forced convective heating did not occur under the panels. After the model was retracted from the flow, the array was allowed to cool.

One objective of the aerothermal tests was to determine whether convective heating occurs in the gaps between panels when the gaps are aligned with the flow. Previous tests on an array of thinner metallic panels with gaps skewed 30° to the flow (ref. 21) revealed no gap heating. The SAHC panels were installed in a worst-case orientation with the gaps parallel to the flow. This orientation may cause hot gas flow to occur in the gaps between panels. Figure 26 shows temperature histories measured during tests 13, 14, 15, and 20 at the bottom of the gaps at sections A-A, B-B, C-C, and D-D (thermocouples 37, 40, 43, and 48, respectively). The temperature histories of thermocouples 37, 40, and 43 (solid lines in fig. 26) show an increase of 400°F at the bottom of the gaps when the array was inserted into the hypersonic flow. This rapid rise in temperature resulted from convective heating caused by hot gas flow in the gaps that contained thermocouple lead wires at the top and the middle of the gap. The presence of the lead wires may have created a hot gas flow path that caused or contributed to the convective heating. However, for each of the four tests, the temperatures sensed by the internally mounted thermocouple (thermocouple 48, shown by dashed lines in fig. 26) did not indicate a rapid temperature rise. Thus, even though forced convective heating occurred in the gaps, the one instrumented gap area without thermocouple wires showed negligible convective heating. Because the existence of thermocouple wires in the gaps between panels may have contributed to the gap heating, a definitive conclusion as to the severity of aerothermal heating in gaps that are parallel to the flow is not possible.

If convective heating in the gaps between panels does occur when the direction of flow over the surface of a vehicle is parallel to the orientation of the gaps between panels, the TPS concept may require modification to eliminate or at least sharply reduce such heating. One proposed modification consists of a beaded Inconel 617 foil bag filled with Cerachrome insulation placed between the side closures of adjacent panels so that it meshes with the beads of the side closure. This compressible

gap-filler design, which is described in reference 22, is lightweight (0.38 lbm/ft^2), is easily brazed to the side closure, and does not interfere with the installation or removal of the panels. Another proposed modification described in reference 22 uses a short foil strip attached at one corner of each panel to block the flow in the gap. However, no such modifications were incorporated or evaluated during these tests.

Before test 20, the surface of the array was intentionally damaged in four places to obtain a qualitative assessment of the effects of a hypersonic flow over different types of surface irregularities that may exist on a TPS panel. These surface irregularities were holes of about 0.5 in. in diameter that represented several types of damage. (See fig. 27.) Impact damage was simulated by grinding the outer face sheet and core and by punching through the outer face sheet and crushing the core. Lightning strike damage (ref. 2) was simulated by burning through only the outer face sheet by gas torch, and accidental loss of an attachment plug was simulated by removing an attachment plug.

Figure 28 shows the effects of aerodynamic heating on the intentionally damaged surface of the model during test 20. The only lighting used to expose the film of the photograph was that radiating from the surface of the array. The surface temperature was about 1850°F. The torch burn-through damage is the bright hot spot on the right side of figure 28. However, the other holes, which were similar in size but deeper, are not apparent in the figure. These results suggest that the appearance of the hot spot was due to the exposure of the honeycomb core to the hypersonic stream.

Additional hot spots at four locations on the array surface (fig. 28) were caused by corners of gap covers (panel overhanging lips) bent up into the flow stream. The corner of the gap cover located near the center of the array may have been pushed up into the flow stream as a result of differences in panel corner rotations that resulted from a unique combination of bayonet-clip attachments and through-panel fasteners at the intersection of the four adjacent panels (panels 1B, 1C, 2B, and 2C, shown in fig. 6). The bent up gap covers along the trailing edge of the array were probably caused by the panels thermally deforming against rigid Glasrock insulation that surrounded the array. The thermal deflections of the heated panels resulted in *pillowing* which caused slightly higher surface temperatures and greater brightness to occur on the upstream side and at the center rather than on the downstream side of individual panels. For example, the maximum temperatures at thermocouples 21 and 22 (fig. 7) were 1760°F and 1850°F, respectively. The greater brightness of the right-hand side of the array was caused by the panels with the noncatalytic coating having a lower emissivity, and thus a higher temperature, than the panels with the high-emissivity black surface coating. (Catalytic reactions were not a factor in these tests because the enthalpy of the Langley 8′HTT is not high enough to cause dissociation.) The hot spots identified as face sheet buckles were due to local separation of the face sheet from the core; this separation was caused by thermal shock when molten glass contacted the panel surface. The molten glass resulted during wind tunnel start-up when fiberglass curtains (which were used to confine radiant heat to the surface of the array during radiant heating tests) contacted the radiant heat lamps, melted, and dripped onto the array surface.

After the array was in the hypersonic flow for about 20 sec during test 20, the bolts holding the lower leading edge cover plate to the panel holder (see fig. 14) failed and allowed the plate to separate from the panel holder. This failure choked the hypersonic flow and caused the tunnel to *unstart*. A strong shock wave of undefined strength (greater than 10 psia rise in 0.2 sec) passed through the test section and over the array. The panels, which were designed to withstand only a pressure load of 2 psi, were completely destroyed by the shock wave. Figure 29 shows the remnants of the array and the locations of panels 1C, 1D, 2C, and 2D. The only components of the array that survived the unstart were the aluminum plate, Nomex felt, and various pieces, such as fastener tubes, vehicle clips, titanium honeycomb sandwich panels, and thermocouple lead wires. Scorching of the Nomex felt strips occurred near the corners of panels and at locations along the edges of some panels. The longitudinal felt strips were more severely scorched than the transverse strips. Although scorching of the felt could have occurred during the radiant heating tests, previous tunnel tests, or unstarting of the hypersonic flow, this scorching pattern suggests that some forced convective heating occurred in the gaps between panels during the tunnel tests. These results support the conclusion stated previously in the discussion of figure 26; that is, forced convective heating caused a rapid gap temperature increase when the model was inserted into the flow.

Concluding Remarks

Superalloy honeycomb (SAHC) metallic thermal protection system (TPS) panels, which were fabricated with foil-gauge Inconel and titanium metals and fiberous insulation, were subjected to thermal, acoustic, and aerothermal tests. The panels had a

mass of 2.201 lbm/ft^2 and could be mechanically attached to the primary structure of an entry vehicle. The purpose of the tests was to assess the viability of the TPS concept and to identify possible shortcomings.

A 2-panel array of SAHC TPS panels was subjected to 26 entry thermal-pressure cycles that simulated a Space Shuttle entry trajectory at a location on the vehicle with a maximum surface temperature of 1900°F. The results from the radiant heating tests and thermal analyses indicate that the TPS panels repeatedly limited the maximum temperature of the aluminum primary structure to well below the design limit of 350°F. The fiberous insulation contained within the panels did not settle or change in appearance after acoustic testing and radiant heating testing. Cracks, observed after completion of the acoustic tests, occurred in one sidewall that was not adequately supported by Nomex felt. No damage occurred on the other seven sides of the two panels, which were properly supported by the Nomex felt. However, a definitive assessment of acoustic life of the TPS panels would require further tests.

Aerothermal test results show that a 20-panel array of SAHC TPS panels can successfully survive the aerodynamic and thermal conditions of a hypersonic flowstream. The panels were installed in a worst-case orientation with the gaps parallel to the flow. This orientation may have caused or contributed to the hot gas flow that occurred in the gaps between the panels. The existence of thermocouple wires in the gaps between panels may have contributed to the gap heating. Proposed design changes to eliminate gap heating include avoiding placement of foreign material (such as thermocouple wires) between panels, orienting panels so that gaps are not parallel to the flow, and using a packaged, compressible *gap-filler* material between panels to block hot gas flow.

Results from these thermal, acoustic, and aerothermal tests show that the SAHC TPS panels can repeatedly endure a realistic entry environment and maintain their effectiveness. The panels limit the primary-structure temperature as designed, have low mass, and exhibit tolerance to damage in an aerothermal environment. Based on these tests, this thermal protection system appears to be a viable candidate for use on future hypersonic vehicles like the Space Shuttle.

NASA Langley Research Center
Hampton, VA 23681-0001
November 24, 1992

References

1. Jackson, L. Robert; and Dixon, Sidney C.: *A Design Assessment of Multiwall, Metallic Stand-Off, and RSI Reusable Thermal Protection Systems Including Space Shuttle Application.* NASA TM-81780, 1980.

2. Shideler, J. L.; Webb, G. L.; and Pittman, C. M.: *Verification Tests of Durable TPS Concepts.* NASA TM-86313, 1984.

3. Burns, A. B.; Banas, R. P.; and Izu, Y. D.: Advanced Ceramic TPS Concepts. *Advances in TPS and Structures for Space Transportation Systems,* H. Neale Kelly and James E. Gardner, compilers, NASA CP-2315, 1984, pp. 239–258.

4. Webb, Granville L.; and Pittman, Claud M.: Design, Fabrication, and Test of a Multipost ACC TPS Concept. *Advances in TPS and Structures for Space Transportation Systems,* H. Neale Kelly and James E. Gardner, compilers, NASA CP-2315, 1984, pp. 489 508.

5. Blair, W.; Meaney, J. E.; and Rosenthal, H. A.: *Fabrication of Prepackaged Superalloy Honeycomb Thermal Protection System (TPS) Panels.* NASA CR-3755, 1985.

6. Blair, Winford: Manufacturing Experiences for Advanced Multiwall and Prepackaged Metallic TPS. *Advances in TPS and Structures for Space Transportation Systems,* H. Neale Kelly and James E. Gardner, compilers, NASA CP-2315, 1984, pp. 261 301.

7. Sawyer, James Wayne: Mechanical Properties of the Shuttle Orbiter Thermal Protection System Strain Isolator Pad. AIAA-82-0789, May 1982.

8. Pittman, Claud M.; Brown, Ronald D.; and Shideler, John L.: *Evaluation of a Non-Catalytic Coating for Metallic TPS.* NASA TM-85745, 1984.

9. Deveikis, William D.; Bruce, Walter E., Jr.; and Karns, John R.: *Techniques for Aerothermal Tests of Large, Flightweight Thermal Protection Panels in a Mach 7 Wind Tunnel.* NASA TM X-71983, 1974.

10. Deveikis, William D.; and Hunt, L. Roane: *Loading and Heating of a Large Flat Plate at Mach 7 in the Langley 8-Foot High-Temperature Structures Tunnel.* NASA TN D-7275, 1973.

11. Marlowe, M. B.; Moore, R. A.; and Whetstone, W. D.: *SPAR Thermal Analysis Processors Reference Manual, System Level 16.* NASA CR-159162, 1979.

12. Brown, William F., Jr.; Mindlin, Harold; and Ho, C. Y.: *Aerospace Structural Metals Handbook—Volume 5, 1992 ed.* (Incorporating Supplements through 1991). CINDAS/Purdue Univ., c.1992.

13. *Military Standardization Handbook Metallic Materials and Elements for Aerospace Vehicle Structures,* Volume 2. MIL-HDBK-5C, U.S. Dep. of Defense, Sept. 15, 1976.

14. Keenan, Joseph H.; Chao, Jing; and Kaye, Joseph: *Gas Tables Thermodynamic Properties of Air Products of Combustion and Component Gases Compressible Flow Functions (Including Those of Ascher H. Shapiro and Gilbert M. Edelman)*, Second ed. (English Units). John Wiley & Sons, Inc., c.1980.

15. Shideler, John L.; Sawyer, James Wayne; Blosser, Max L.; and Webb, Granville L.: *Multiwall/RSI Concept for Local Application to Space Shuttle Body Flap.* NASA TM-87589, 1985.

16. Kreith, Frank; and Black, William Z.: *Basic Heat Transfer.* Harper & Row, Publ., c.1980.

17. Hays, D.: *An Assessment of Alternate Thermal Protection Systems for the Space Shuttle Orbiter.* NASA CR-165790, 1982.

18. Ho, T.; and Allsup, H. C.: *ACC Heat Shield Viability.* NASA CR-177934, 1985.

19. *Aerospace Insulation Q-Fiber® Felt.* A1-8, Manville Products Corp., Sept. 1982.

20. *Refractory Products Cerachrome™ Blanket.* R-510, Sec. 120, Pt. 20, Manville Products Corp., Mar. 1984. (Cancels Aug. 1983.)

21. Avery, Don E.; Shideler, John L.; and Stuckey, Robert N.: *Thermal and Aerothermal Performance of a Titanium Multiwall Thermal Protection System.* NASA TP-1961, 1981.

22. Anderson, J.; LeHolm, R. B.; Meaney, J. E.; and Rosenthal, H. A.: *Development of Reusable Metallic Thermal Protection System Panels for Entry Vehicles.* NASA CR-181783, 1989.

Table I. Test Summary for Two-Panel Array

Test cycle	Type of test	Conditions	Comments
0	Coating cure	500°F	Surface coating cure
1–16	Radiant heating	1900°F	Design entry temperature and pressure conditions
Post cycle 16	Acoustic	15 min, 161 dB	Acoustic conditions representative of 25 missions
17–25	Radiant heating	1900°F	Design entry temperature and pressure conditions
26	Radiant heating	2000°F	Design entry over-temperature and pressure conditions

Table II. Test Summary for 20-Panel Array in Langley 8-Foot High-Temperature Tunnel

Test cycle	Type of test	Nominal maximum surface temperature, °F	Comments
1–2	Heat lamp adjustment		No radiant heating of panels
3–6	Coating cure	500	Surface coating cure
7–8	Radiant heating	1900	Array surface radiantly heated to 1900°F and held for 200 sec
9	Radiant heating	2000	Array surface radiantly heated to 2000°F and held for 200 sec
10–11	Radiant preheating	1900	Array surface radiantly preheated; tunnel did not start
12	Wind tunnel		Tunnel check-out run; no array heating or insertion
13	Aerothermal	1900	Array in flow for 20 sec
14	Aerothermal	1900	Array in flow for 7 sec
15	Aerothermal	1900	Array in flow for 18 sec
16–17	Aerothermal		Wedge, positioned above array to induce shock impingement, prevented preheating the array. Panel thermal expansion did not close gaps; data are of academic interest only
18–19	Radiant preheating	2000	Array surface radiantly preheated; tunnel did not start
20	Aerothermal	2000	Array in flow for 20 sec; tunnel flow broke down; model was destroyed as a result of a high-pressure shock

Table III. Wind Tunnel Test Conditions for Aerothermal Tests

Test	Combustor temperature, °F	Combustor pressure, psia	Free-stream Mach number	Local Mach number	Free-stream dynamic pressure, psi	Free-stream Reynolds number, ft^{-1}	Angle of attack, deg
13	3000	3000	6.75	4.12	11.37	1.68×10^6	16.8
14	3000	3000	6.75	4.17	11.37	1.68	16.4
15	3000	3000	6.75	4.12	11.37	1.68	16.8
20	3000	3000	6.75	4.19	11.37	1.68	16.3

Table IV. Thermophysical Properties of Materials Used in Analysis

Temperature, °R	Density, lbm/in^3	Specific heat, Btu/lbm	Thermal conductivity, Btu/(sec-in-°R)		
			x-direction	y-direction	z-direction
Inconel 617 honeycomb-core sandwich					
460.0	0.01505	9.7440×10^{-2}	5.2756×10^{-6}	3.0045×10^{-6}	5.2756×10^{-6}
560.0	0.01505	0.1007	5.8985×10^{-6}	3.4305×10^{-6}	5.8985×10^{-6}
660.0	0.01505	0.1040	6.6299×10^{-6}	3.8565×10^{-6}	6.6299×10^{-6}
860.0	0.01505	0.1110	7.9782×10^{-6}	4.7245×10^{-6}	7.9782×10^{-6}
1060.0	0.01505	0.1170	9.3241×10^{-6}	5.8148×10^{-6}	9.3241×10^{-6}
1260.0	0.01505	0.1240	1.0671×10^{-5}	7.1921×10^{-6}	1.0671×10^{-5}
1460.0	0.01505	0.1310	1.2014×10^{-5}	8.9028×10^{-6}	1.2014×10^{-5}
1660.0	0.01505	0.1370	1.3326×10^{-5}	1.1007×10^{-5}	1.3326×10^{-5}
1860.0	0.01505	0.1440	1.4682×10^{-5}	1.3560×10^{-5}	1.4682×10^{-5}
2060.0	0.01505	0.1500	1.6006×10^{-5}	1.6616×10^{-5}	1.6006×10^{-5}
2260.0	0.01505	0.1566	1.7327×10^{-5}	2.0227×10^{-5}	1.7327×10^{-5}
2470.0	0.01505	0.1630	1.8651×10^{-5}	2.4456×10^{-5}	1.8651×10^{-5}
Air					
500.0	4.6878×10^{-7}	0.2396	3.3102×10^{-7}	3.3102×10^{-7}	3.3102×10^{-7}
600.0	4.6878×10^{-7}	0.2403	3.8889×10^{-7}	3.8889×10^{-7}	3.8889×10^{-7}
800.0	4.6878×10^{-7}	0.2434	4.9306×10^{-7}	4.9306×10^{-7}	4.9306×10^{-7}
1000.0	4.6878×10^{-7}	0.2486	6.0185×10^{-7}	6.0185×10^{-7}	6.0185×10^{-7}
1200.0	4.6878×10^{-7}	0.2547	6.9444×10^{-7}	6.9444×10^{-7}	6.9444×10^{-7}
1400.0	4.6878×10^{-7}	0.2611	8.1019×10^{-7}	8.1019×10^{-7}	8.1019×10^{-7}
1600.0	4.6878×10^{-7}	0.2671	9.0278×10^{-7}	9.0278×10^{-7}	9.0278×10^{-7}
1800.0	4.6878×10^{-7}	0.2725	9.9537×10^{-7}	9.9537×10^{-7}	9.9537×10^{-7}
2000.0	4.6878×10^{-7}	0.2773	1.0648×10^{-6}	1.0648×10^{-6}	1.0648×10^{-6}
2200.0	4.6878×10^{-7}	0.2813	1.1574×10^{-6}	1.1574×10^{-6}	1.1574×10^{-6}
2400.0	4.6878×10^{-7}	0.2848	1.2269×10^{-6}	1.2269×10^{-6}	1.2269×10^{-6}
2600.0	4.6878×10^{-7}	0.2878	1.3079×10^{-6}	1.3079×10^{-6}	1.3079×10^{-6}
Inconel 617 foil sheet					
520.0	0.3015	0.1000	1.8287×10^{-4}		
1460.0	0.3015	0.1310	2.8704×10^{-4}		
2470.0	0.3015	0.1630	4.0278×10^{-4}		
Aluminum					
460.0	0.1010	0.1950	1.50×10^{-3}	1.50×10^{-3}	1.50×10^{-3}
560.0	0.1010	0.2060	1.67×10^{-3}	1.67×10^{-3}	1.67×10^{-3}
660.0	0.1010	0.2160	1.85×10^{-3}	1.85×10^{-3}	1.85×10^{-3}
760.0	0.1010	0.2240	2.07×10^{-3}	2.07×10^{-3}	2.07×10^{-3}
860.0	0.1010	0.2370	2.29×10^{-3}	2.29×10^{-3}	2.29×10^{-3}
960.0	0.1010	0.2420	2.39×10^{-3}	2.39×10^{-3}	2.39×10^{-3}
1060.0	0.1010	0.2500	2.42×10^{-3}	2.42×10^{-3}	2.42×10^{-3}
1660.0	0.1010	0.3070	3.46×10^{-3}	3.46×10^{-3}	3.46×10^{-3}

Table IV. Continued

Temperature, °R	Density, lbm/in^3	Specific heat, Btu/lbm	Thermal conductivity, Btu/(sec-in-°R)		
			x-direction	y-direction	z-direction
Titanium honeycomb-core sandwich					
460.0	0.01399	0.1400	7.7472×10^{-6}	1.5069×10^{-6}	7.7472×10^{-6}
560.0	0.01399	0.1400	7.7928×10^{-6}	1.7685×10^{-6}	7.7928×10^{-6}
660.0	0.01399	0.1400	7.9397×10^{-6}	2.0440×10^{-6}	7.9397×10^{-6}
860.0	0.01399	0.1450	9.1790×10^{-6}	2.6227×10^{-6}	9.1790×10^{-6}
1060.0	0.01399	0.1480	1.0592×10^{-5}	3.2708×10^{-6}	1.0592×10^{-5}
1260.0	0.01399	0.1550	1.2006×10^{-5}	4.0602×10^{-6}	1.2006×10^{-5}
1460.0	0.01399	0.1660	1.3469×10^{-5}	4.9745×10^{-6}	1.3469×10^{-5}
1960.0	0.01399	0.1800	1.7031×10^{-5}	6.4954×10^{-6}	1.7031×10^{-5}
2470.0	0.01399	0.1978	2.0620×10^{-5}	8.2320×10^{-6}	2.0620×10^{-5}
Q-Fiber felt insulation; Pressure = 7.5486×10^{-5} psia					
460.0	2.0255×10^{-3}	0.1808	5.9374×10^{-8}	4.3981×10^{-8}	5.9374×10^{-8}
560.0	2.0255×10^{-3}	0.1913	5.9374×10^{-8}	4.3981×10^{-8}	5.9374×10^{-8}
660.0	2.0255×10^{-3}	0.2018	1.5313×10^{-7}	1.1343×10^{-7}	1.5313×10^{-7}
760.0	2.0255×10^{-3}	0.2113	2.4062×10^{-7}	1.7824×10^{-7}	2.4062×10^{-7}
860.0	2.0255×10^{-3}	0.2268	3.3125×10^{-7}	2.4537×10^{-7}	3.3125×10^{-7}
1060.0	2.0255×10^{-3}	0.2466	5.6562×10^{-7}	4.1898×10^{-7}	5.6562×10^{-7}
1260.0	2.0255×10^{-3}	0.2636	8.3438×10^{-7}	6.1806×10^{-7}	8.3438×10^{-7}
1460.0	2.0255×10^{-3}	0.2726	1.1375×10^{-6}	8.4259×10^{-7}	1.1375×10^{-6}
1660.0	2.0255×10^{-3}	0.2788	1.4876×10^{-6}	1.1019×10^{-6}	1.4876×10^{-6}
1860.0	2.0255×10^{-3}	0.2811	1.9468×10^{-6}	1.4421×10^{-6}	1.9468×10^{-6}
1960.0	2.0255×10^{-3}	0.2827	2.3906×10^{-6}	1.7708×10^{-6}	2.3906×10^{-6}
2060.0	2.0255×10^{-3}	0.2844	2.8312×10^{-6}	2.0972×10^{-6}	2.8312×10^{-6}
2470.0	2.0255×10^{-3}	0.2910	4.6005×10^{-6}	3.4078×10^{-6}	4.6005×10^{-6}
Q-Fiber felt insulation; Pressure = 1.9306×10^{-4} psia					
460.0	2.0255×10^{-3}	0.1808	6.2500×10^{-8}	4.6296×10^{-8}	6.2500×10^{-8}
560.0	2.0255×10^{-3}	0.1913	6.2500×10^{-8}	4.6296×10^{-8}	6.2500×10^{-8}
660.0	2.0255×10^{-3}	0.2018	1.5625×10^{-7}	1.1574×10^{-7}	1.5625×10^{-7}
760.0	2.0255×10^{-3}	0.2113	2.4376×10^{-7}	1.8056×10^{-7}	2.4376×10^{-7}
860.0	2.0255×10^{-3}	0.2268	3.3438×10^{-7}	2.4769×10^{-7}	3.3438×10^{-7}
1060.0	2.0255×10^{-3}	0.2466	5.6562×10^{-7}	4.1898×10^{-7}	5.6562×10^{-7}
1260.0	2.0255×10^{-3}	0.2636	8.3438×10^{-7}	6.1806×10^{-7}	8.3438×10^{-7}
1460.0	2.0255×10^{-3}	0.2726	8.4259×10^{-7}	8.4259×10^{-7}	8.4259×10^{-7}
1660.0	2.0255×10^{-3}	0.2788	1.4876×10^{-6}	1.1019×10^{-6}	1.4876×10^{-6}
1860.0	2.0255×10^{-3}	0.2811	1.9499×10^{-6}	1.4444×10^{-6}	1.9499×10^{-6}
1960.0	2.0255×10^{-3}	0.2827	2.3906×10^{-6}	1.7708×10^{-6}	2.3906×10^{-6}
2060.0	2.0255×10^{-3}	0.2844	2.8312×10^{-6}	2.0972×10^{-6}	2.8312×10^{-6}
2470.0	2.0255×10^{-3}	0.2910	4.5938×10^{-6}	3.4028×10^{-6}	4.5938×10^{-6}

Table IV. Continued

Temperature, °R	Density, lbm/in^3	Specific heat, Btu/lbm	Thermal conductivity, Btu/(sec-in-°R)		
			x-direction	y-direction	z-direction
Q-Fiber felt insulation; Pressure = 1.9340×10^{-3} psia					
460.0	2.0255×10^{-3}	0.1808	9.3749×10^{-8}	6.9444×10^{-8}	9.3749×10^{-8}
560.0	2.0255×10^{-3}	0.1913	9.3749×10^{-8}	6.9444×10^{-8}	9.3749×10^{-8}
660.0	2.0255×10^{-3}	0.2018	1.8437×10^{-7}	1.3657×10^{-7}	1.8437×10^{-7}
760.0	2.0255×10^{-3}	0.2113	2.7188×10^{-7}	2.0139×10^{-7}	2.7188×10^{-7}
860.0	2.0255×10^{-3}	0.2268	3.6250×10^{-7}	2.6852×10^{-7}	3.6250×10^{-7}
1060.0	2.0255×10^{-3}	0.2466	5.8751×10^{-7}	4.3519×10^{-7}	5.8751×10^{-7}
1260.0	2.0255×10^{-3}	0.2636	8.5625×10^{-7}	6.3426×10^{-7}	8.5625×10^{-7}
1460.0	2.0255×10^{-3}	0.2726	1.1562×10^{-6}	8.5648×10^{-7}	1.1562×10^{-6}
1660.0	2.0255×10^{-3}	0.2788	1.5094×10^{-6}	1.1181×10^{-6}	1.5094×10^{-6}
1860.0	2.0255×10^{-3}	0.2811	1.9844×10^{-6}	1.4699×10^{-6}	1.9844×10^{-6}
1960.0	2.0255×10^{-3}	0.2827	2.4062×10^{-6}	1.7824×10^{-6}	2.4062×10^{-6}
2060.0	2.0255×10^{-3}	0.2844	2.8281×10^{-6}	2.0949×10^{-6}	2.8281×10^{-6}
2470.0	2.0255×10^{-3}	0.2910	4.5156×10^{-6}	3.3449×10^{-6}	4.5156×10^{-6}
Q-Fiber felt insulation; Pressure = 1.9340×10^{-2} psia					
460.0	2.0255×10^{-3}	0.1808	2.6563×10^{-7}	1.9676×10^{-7}	2.6563×10^{-7}
560.0	2.0255×10^{-3}	0.1913	2.6563×10^{-7}	1.9676×10^{-7}	2.6563×10^{-7}
660.0	2.0255×10^{-3}	0.2018	3.6250×10^{-7}	2.6852×10^{-7}	3.6250×10^{-7}
760.0	2.0255×10^{-3}	0.2113	4.5313×10^{-7}	3.3565×10^{-7}	4.5313×10^{-7}
860.0	2.0255×10^{-3}	0.2268	5.4375×10^{-7}	4.0278×10^{-7}	5.4375×10^{-7}
1060.0	2.0255×10^{-3}	0.2466	7.6874×10^{-7}	5.6944×10^{-7}	7.6874×10^{-7}
1260.0	2.0255×10^{-3}	0.2636	1.0313×10^{-6}	7.6389×10^{-7}	1.0313×10^{-6}
1460.0	2.0255×10^{-3}	0.2726	1.3281×10^{-6}	9.8380×10^{-7}	1.3281×10^{-6}
1660.0	2.0255×10^{-3}	0.2788	1.6687×10^{-6}	1.2361×10^{-6}	1.6687×10^{-6}
1860.0	2.0255×10^{-3}	0.2811	2.1406×10^{-6}	1.5856×10^{-6}	2.1406×10^{-6}
1960.0	2.0255×10^{-3}	0.2827	2.5624×10^{-6}	1.8981×10^{-6}	2.5624×10^{-6}
2060.0	2.0255×10^{-3}	0.2844	2.9843×10^{-6}	2.2106×10^{-6}	2.9843×10^{-6}
2470.0	2.0255×10^{-3}	0.2910	4.6718×10^{-6}	3.4606×10^{-6}	4.6718×10^{-6}
Q-Fiber felt insulation; Pressure = 1.9340×10^{-1} psia					
460.0	2.0255×10^{-3}	0.1808	4.8438×10^{-7}	3.5880×10^{-7}	4.8438×10^{-7}
560.0	2.0255×10^{-3}	0.1913	4.8438×10^{-7}	3.5880×10^{-7}	4.8438×10^{-7}
660.0	2.0255×10^{-3}	0.2018	6.2813×10^{-7}	4.6528×10^{-7}	6.2813×10^{-7}
760.0	2.0255×10^{-3}	0.2113	7.6249×10^{-7}	5.6481×10^{-7}	7.6249×10^{-7}
860.0	2.0255×10^{-3}	0.2268	8.9062×10^{-7}	6.5972×10^{-7}	8.9062×10^{-7}
1060.0	2.0255×10^{-3}	0.2466	1.1875×10^{-6}	8.7963×10^{-7}	1.1875×10^{-6}
1260.0	2.0255×10^{-3}	0.2636	1.5094×10^{-6}	1.1181×10^{-6}	1.5094×10^{-6}
1460.0	2.0255×10^{-3}	0.2726	1.8500×10^{-6}	1.3704×10^{-6}	1.8500×10^{-6}
1660.0	2.0255×10^{-3}	0.2788	2.2282×10^{-6}	1.6505×10^{-6}	2.2282×10^{-6}
1860.0	2.0255×10^{-3}	0.2811	2.7375×10^{-6}	2.0278×10^{-6}	2.7375×10^{-6}
1960.0	2.0255×10^{-3}	0.2827	3.1718×10^{-6}	2.3495×10^{-6}	3.1718×10^{-6}
2060.0	2.0255×10^{-3}	0.2844	3.6063×10^{-6}	2.6713×10^{-6}	3.6063×10^{-6}
2470.0	2.0255×10^{-3}	0.2910	5.3437×10^{-6}	3.9583×10^{-6}	5.3437×10^{-6}

Table IV. Continued

Temperature, °R	Density, lbm/in^3	Specific heat, Btu/lbm	Thermal conductivity, Btu/(sec-in-°R)		
			x-direction	y-direction	z-direction
Q-Fiber felt insulation; Pressure = 9.6667×10^{-1} psia					
460.0	2.0255×10^{-3}	0.1808	5.2500×10^{-7}	3.8889×10^{-7}	5.2500×10^{-7}
560.0	2.0255×10^{-3}	0.1913	5.2500×10^{-7}	3.8889×10^{-7}	5.2500×10^{-7}
660.0	2.0255×10^{-3}	0.2018	6.8750×10^{-7}	5.0926×10^{-7}	6.8750×10^{-7}
760.0	2.0255×10^{-3}	0.2113	8.3750×10^{-7}	6.2037×10^{-7}	8.3750×10^{-7}
860.0	2.0255×10^{-3}	0.2268	9.8750×10^{-7}	7.3148×10^{-7}	9.8750×10^{-7}
1060.0	2.0255×10^{-3}	0.2466	1.3281×10^{-6}	9.8380×10^{-7}	1.3281×10^{-6}
1260.0	2.0255×10^{-3}	0.2636	1.6906×10^{-6}	1.2523×10^{-6}	1.6906×10^{-6}
1460.0	2.0255×10^{-3}	0.2726	2.0782×10^{-6}	1.5394×10^{-6}	2.0782×10^{-6}
1660.0	2.0255×10^{-3}	0.2788	2.5063×10^{-6}	1.8565×10^{-6}	2.5063×10^{-6}
1860.0	2.0255×10^{-3}	0.2811	3.0656×10^{-6}	2.2708×10^{-6}	3.0656×10^{-6}
1960.0	2.0255×10^{-3}	0.2827	3.5219×10^{-6}	2.6088×10^{-6}	3.5219×10^{-6}
2060.0	2.0255×10^{-3}	0.2844	3.9782×10^{-6}	2.9468×10^{-6}	3.9782×10^{-6}
2470.0	2.0255×10^{-3}	0.2910	5.8034×10^{-6}	4.2988×10^{-6}	5.8034×10^{-6}
Q-Fiber felt insulation; Pressure = 1.9333 psia					
460.0	2.0255×10^{-3}	0.1808	5.3125×10^{-7}	3.9352×10^{-7}	5.3125×10^{-7}
560.0	2.0255×10^{-3}	0.1913	5.3125×10^{-7}	3.9352×10^{-7}	5.3125×10^{-7}
660.0	2.0255×10^{-3}	0.2018	6.9687×10^{-7}	5.1620×10^{-7}	6.9687×10^{-7}
760.0	2.0255×10^{-3}	0.2113	8.5000×10^{-7}	6.2963×10^{-7}	8.5000×10^{-7}
860.0	2.0255×10^{-3}	0.2268	1.0031×10^{-6}	7.4306×10^{-7}	1.0031×10^{-6}
1060.0	2.0255×10^{-3}	0.2466	1.3500×10^{-6}	1.0000×10^{-6}	1.3500×10^{-6}
1260.0	2.0255×10^{-3}	0.2636	1.7219×10^{-6}	1.2755×10^{-6}	1.7219×10^{-6}
1460.0	2.0255×10^{-3}	0.2726	2.1187×10^{-6}	1.5694×10^{-6}	2.1187×10^{-6}
1660.0	2.0255×10^{-3}	0.2788	2.5562×10^{-6}	1.8935×10^{-6}	2.5562×10^{-6}
1860.0	2.0255×10^{-3}	0.2811	3.1281×10^{-6}	2.3171×10^{-6}	3.1281×10^{-6}
1960.0	2.0255×10^{-3}	0.2827	3.5906×10^{-6}	2.6597×10^{-6}	3.5906×10^{-6}
2060.0	2.0255×10^{-3}	0.2844	4.0531×10^{-6}	3.0023×10^{-6}	4.0531×10^{-6}
2470.0	2.0255×10^{-3}	0.2910	5.9031×10^{-6}	4.3727×10^{-6}	5.9031×10^{-6}
Q-Fiber felt insulation; Pressure = 1.4700×10^{1} psia					
460.0	2.0255×10^{-3}	0.1808	5.3750×10^{-7}	3.9815×10^{-7}	5.3750×10^{-7}
560.0	2.0255×10^{-3}	0.1913	5.3750×10^{-7}	3.9815×10^{-7}	5.3750×10^{-7}
660.0	2.0255×10^{-3}	0.2018	7.0312×10^{-7}	5.2083×10^{-7}	7.0312×10^{-7}
760.0	2.0255×10^{-3}	0.2113	8.5937×10^{-7}	6.3657×10^{-7}	8.5937×10^{-7}
860.0	2.0255×10^{-3}	0.2268	1.0156×10^{-6}	7.5231×10^{-7}	1.0156×10^{-7}
1060.0	2.0255×10^{-3}	0.2466	1.3688×10^{-6}	1.0139×10^{-6}	1.3688×10^{-6}
1260.0	2.0255×10^{-3}	0.2636	1.7500×10^{-6}	1.2963×10^{-6}	1.7500×10^{-6}
1460.0	2.0255×10^{-3}	0.2726	2.1562×10^{-6}	1.5972×10^{-6}	2.1562×10^{-6}
1660.0	2.0255×10^{-3}	0.2788	2.6031×10^{-6}	1.9282×10^{-6}	2.6031×10^{-6}
1860.0	2.0255×10^{-3}	0.2811	3.1875×10^{-6}	2.3611×10^{-6}	3.1875×10^{-6}
1960.0	2.0255×10^{-3}	0.2827	3.6562×10^{-6}	2.7083×10^{-6}	3.6562×10^{-6}
2060.0	2.0255×10^{-3}	0.2844	4.1251×10^{-6}	3.0556×10^{-6}	4.1251×10^{-6}
2470.0	2.0255×10^{-3}	0.2910	6.0002×10^{-6}	4.4446×10^{-6}	6.0002×10^{-6}

Table IV. Continued

Temperature, °R	Density, lbm/in^3	Specific heat, Btu/lbm	Thermal conductivity, Btu/(sec-in-°R)		
			x-direction	y-direction	z-direction
Cerachrome insulation; Pressure = 7.5486×10^{-5} psia					
460.0	3.4722×10^{-3}	0.1648	1.3437×10^{-7}	9.9537×10^{-8}	1.3437×10^{-7}
660.0	3.4722×10^{-3}	0.1958	1.3437×10^{-7}	9.9537×10^{-8}	1.3437×10^{-7}
860.0	3.4722×10^{-3}	0.2268	3.3125×10^{-7}	2.4537×10^{-7}	3.3125×10^{-7}
1060.0	3.4722×10^{-3}	0.2482	5.4062×10^{-7}	4.0046×10^{-7}	5.4062×10^{-7}
1260.0	3.4722×10^{-3}	0.2640	7.9688×10^{-7}	5.9028×10^{-7}	7.9688×10^{-7}
1460.0	3.4722×10^{-3}	0.2726	1.1531×10^{-6}	8.5417×10^{-7}	1.1531×10^{-6}
1660.0	3.4722×10^{-3}	0.2789	1.6563×10^{-6}	1.2269×10^{-6}	1.6563×10^{-6}
1860.0	3.4722×10^{-3}	0.2808	2.2063×10^{-6}	1.6343×10^{-6}	2.2063×10^{-6}
2060.0	3.4722×10^{-3}	0.2839	2.9063×10^{-6}	2.1528×10^{-6}	2.9063×10^{-6}
2260.0	3.4722×10^{-3}	0.2871	3.6123×10^{-6}	2.6758×10^{-6}	3.6123×10^{-6}
2460.0	3.4722×10^{-3}	0.2902	4.5812×10^{-6}	3.3935×10^{-6}	4.5812×10^{-6}
2660.0	3.4722×10^{-3}	0.2934	5.7094×10^{-6}	4.2292×10^{-6}	5.7094×10^{-6}
2860.0	3.4722×10^{-3}	0.2965	6.7906×10^{-6}	5.0301×10^{-6}	6.7906×10^{-6}
Cerachrome insulation; Pressure = 1.9306×10^{-4} psia					
460.0	3.4722×10^{-3}	0.1648	1.3437×10^{-7}	9.9537×10^{-8}	1.3437×10^{-7}
660.0	3.4722×10^{-3}	0.1958	1.3437×10^{-7}	9.9537×10^{-8}	1.3437×10^{-7}
860.0	3.4722×10^{-3}	0.2268	3.3125×10^{-7}	2.4537×10^{-7}	3.3125×10^{-7}
1060.0	3.4722×10^{-3}	0.2482	5.4062×10^{-7}	4.0046×10^{-7}	5.4062×10^{-7}
1260.0	3.4722×10^{-3}	0.2640	7.9688×10^{-7}	5.9028×10^{-7}	7.9688×10^{-7}
1460.0	3.4722×10^{-3}	0.2726	1.1531×10^{-6}	8.5417×10^{-7}	1.1531×10^{-6}
1660.0	3.4722×10^{-3}	0.2789	1.6563×10^{-6}	1.2269×10^{-6}	1.6563×10^{-6}
1860.0	3.4722×10^{-3}	0.2808	2.2063×10^{-6}	1.6343×10^{-6}	2.2063×10^{-6}
2060.0	3.4722×10^{-3}	0.2839	2.9063×10^{-6}	2.1528×10^{-6}	2.9063×10^{-6}
2260.0	3.4722×10^{-3}	0.2871	3.6123×10^{-6}	2.6758×10^{-6}	3.6123×10^{-6}
2460.0	3.4722×10^{-3}	0.2902	4.5812×10^{-6}	3.3935×10^{-6}	4.5812×10^{-6}
2660.0	3.4722×10^{-3}	0.2934	5.7094×10^{-6}	4.2292×10^{-6}	5.7094×10^{-6}
2860.0	3.4722×10^{-3}	0.2965	6.7906×10^{-6}	5.0301×10^{-6}	6.7906×10^{-6}
Cerachrome insulation; Pressure = 1.9340×10^{-3} psia					
460.0	3.4722×10^{-3}	0.1648	1.5000×10^{-7}	1.1111×10^{-7}	1.5000×10^{-7}
660.0	3.4722×10^{-3}	0.1958	1.5000×10^{-7}	1.1111×10^{-7}	1.5000×10^{-7}
860.0	3.4722×10^{-3}	0.2268	3.4687×10^{-7}	2.5694×10^{-7}	3.4687×10^{-7}
1060.0	3.4722×10^{-3}	0.2482	5.5312×10^{-7}	4.0972×10^{-7}	5.5312×10^{-7}
1260.0	3.4722×10^{-3}	0.2640	8.0938×10^{-7}	5.9954×10^{-7}	8.0938×10^{-7}
1460.0	3.4722×10^{-3}	0.2726	1.1656×10^{-6}	8.6343×10^{-7}	1.1656×10^{-6}
1660.0	3.4722×10^{-3}	0.2789	1.6687×10^{-6}	1.2361×10^{-6}	1.6687×10^{-6}
1860.0	3.4722×10^{-3}	0.2808	2.2187×10^{-6}	1.6435×10^{-6}	2.2187×10^{-6}
2060.0	3.4722×10^{-3}	0.2839	2.9156×10^{-6}	2.1597×10^{-6}	2.9156×10^{-6}
2260.0	3.4722×10^{-3}	0.2871	3.6219×10^{-6}	2.6829×10^{-6}	3.6219×10^{-6}
2460.0	3.4722×10^{-3}	0.2902	4.5907×10^{-6}	3.4005×10^{-6}	4.5907×10^{-6}
2660.0	3.4722×10^{-3}	0.2934	5.7156×10^{-6}	4.2338×10^{-6}	5.7156×10^{-6}
2860.0	3.4722×10^{-3}	0.2965	6.7968×10^{-6}	5.0347×10^{-6}	6.7968×10^{-6}

Table IV. Continued

Temperature, °R	Density, lbm/in^3	Specific heat, Btu/lbm	Thermal conductivity, Btu/(sec-in-°R)		
			x-direction	y-direction	z-direction
Cerachrome insulation; Pressure = 1.9340×10^{-2} psia					
460.0	3.4722×10^{-3}	0.1648	2.7500×10^{-7}	2.0370×10^{-7}	2.7500×10^{-7}
660.0	3.4722×10^{-3}	0.1958	2.7500×10^{-7}	2.0370×10^{-7}	2.7500×10^{-7}
860.0	3.4722×10^{-3}	0.2268	4.6875×10^{-7}	3.4722×10^{-7}	4.6875×10^{-7}
1060.0	3.4722×10^{-3}	0.2482	6.6875×10^{-7}	4.9537×10^{-7}	6.6875×10^{-7}
1260.0	3.4722×10^{-3}	0.2640	9.1876×10^{-7}	6.8056×10^{-7}	9.1876×10^{-7}
1460.0	3.4722×10^{-3}	0.2726	1.2687×10^{-6}	9.3981×10^{-7}	1.2687×10^{-6}
1660.0	3.4722×10^{-3}	0.2789	1.7688×10^{-6}	1.3102×10^{-6}	1.7688×10^{-6}
1860.0	3.4722×10^{-3}	0.2808	2.3126×10^{-6}	1.7130×10^{-6}	2.3126×10^{-6}
2060.0	3.4722×10^{-3}	0.2839	3.0063×10^{-6}	2.2269×10^{-6}	3.0063×10^{-6}
2260.0	3.4722×10^{-3}	0.2871	3.7094×10^{-6}	2.7477×10^{-6}	3.7094×10^{-6}
2460.0	3.4722×10^{-3}	0.2902	4.6751×10^{-6}	3.4630×10^{-6}	4.6751×10^{-6}
2660.0	3.4722×10^{-3}	0.2934	5.7969×10^{-6}	4.2940×10^{-6}	5.7969×10^{-6}
2860.0	3.4722×10^{-3}	0.2965	6.8750×10^{-6}	5.0926×10^{-6}	6.8750×10^{-6}
Cerachrome insulation; Pressure = 1.9340×10^{-1} psia					
460.0	3.4722×10^{-3}	0.1648	5.5625×10^{-7}	4.1204×10^{-7}	5.5625×10^{-7}
660.0	3.4722×10^{-3}	0.1958	5.5625×10^{-7}	4.1204×10^{-7}	5.5625×10^{-7}
860.0	3.4722×10^{-3}	0.2268	8.1563×10^{-7}	6.0417×10^{-7}	8.1563×10^{-7}
1060.0	3.4722×10^{-3}	0.2482	1.0688×10^{-6}	7.9167×10^{-7}	1.0688×10^{-6}
1260.0	3.4722×10^{-3}	0.2640	1.3531×10^{-6}	1.0023×10^{-6}	1.3531×10^{-6}
1460.0	3.4722×10^{-3}	0.2726	1.7281×10^{-6}	1.2801×10^{-6}	1.7281×10^{-6}
1660.0	3.4722×10^{-3}	0.2789	2.2437×10^{-6}	1.6620×10^{-6}	2.2437×10^{-6}
1860.0	3.4722×10^{-3}	0.2808	2.8000×10^{-6}	2.0741×10^{-6}	2.8000×10^{-6}
2060.0	3.4722×10^{-3}	0.2839	3.4969×10^{-6}	2.5903×10^{-6}	3.4969×10^{-6}
2260.0	3.4722×10^{-3}	0.2871	4.2031×10^{-6}	3.1134×10^{-6}	4.2031×10^{-6}
2460.0	3.4722×10^{-3}	0.2902	5.1687×10^{-6}	3.8287×10^{-6}	5.1687×10^{-6}
2660.0	3.4722×10^{-3}	0.2934	6.2906×10^{-6}	4.6597×10^{-6}	6.2906×10^{-6}
2860.0	3.4722×10^{-3}	0.2965	7.3687×10^{-6}	5.4583×10^{-6}	7.3687×10^{-6}
Cerachrome insulation; Pressure = 9.6667×10^{-1} psia					
460.0	3.4722×10^{-3}	0.1648	6.4375×10^{-7}	4.7685×10^{-7}	6.4375×10^{-7}
660.0	3.4722×10^{-3}	0.1958	6.4375×10^{-7}	4.7685×10^{-7}	6.4375×10^{-7}
860.0	3.4722×10^{-3}	0.2268	9.5625×10^{-7}	7.0833×10^{-7}	9.5625×10^{-7}
1060.0	3.4722×10^{-3}	0.2482	1.2594×10^{-6}	9.3287×10^{-7}	1.2594×10^{-6}
1260.0	3.4722×10^{-3}	0.2640	1.6000×10^{-6}	1.1852×10^{-6}	1.6000×10^{-6}
1460.0	3.4722×10^{-3}	0.2726	2.0281×10^{-6}	1.5023×10^{-6}	2.0281×10^{-6}
1660.0	3.4722×10^{-3}	0.2789	2.5938×10^{-6}	1.9213×10^{-6}	2.5938×10^{-6}
1860.0	3.4722×10^{-3}	0.2808	3.1969×10^{-6}	2.3681×10^{-6}	3.1969×10^{-6}
2060.0	3.4722×10^{-3}	0.2839	3.9438×10^{-6}	2.9213×10^{-6}	3.9438×10^{-6}
2260.0	3.4722×10^{-3}	0.2871	4.6906×10^{-6}	3.4745×10^{-6}	4.6906×10^{-6}
2460.0	3.4722×10^{-3}	0.2902	5.6969×10^{-6}	4.2199×10^{-6}	5.6969×10^{-6}
2660.0	3.4722×10^{-3}	0.2934	6.8531×10^{-6}	5.0764×10^{-6}	6.8531×10^{-6}
2860.0	3.4722×10^{-3}	0.2965	7.9657×10^{-6}	5.9005×10^{-6}	7.9657×10^{-6}

Table IV. Concluded

Temperature, °R	Density, lbm/in^3	Specific heat, Btu/lbm	Thermal conductivity, Btu/(sec-in-°R)		
			x-direction	y-direction	z-direction
Cerachrome insulation; Pressure = 1.9333 psia					
460.0	3.4722×10^{-3}	0.1648	6.5938×10^{-7}	4.8843×10^{-7}	6.5938×10^{-7}
660.0	3.4722×10^{-3}	0.1958	6.5938×10^{-7}	4.8843×10^{-7}	6.5938×10^{-7}
860.0	3.4722×10^{-3}	0.2268	9.7813×10^{-7}	7.2454×10^{-7}	9.7813×10^{-7}
1060.0	3.4722×10^{-3}	0.2482	1.2937×10^{-6}	9.5833×10^{-7}	1.2937×10^{-6}
1260.0	3.4722×10^{-3}	0.2640	1.6469×10^{-6}	1.2199×10^{-6}	1.6469×10^{-6}
1460.0	3.4722×10^{-3}	0.2726	2.0906×10^{-6}	1.5486×10^{-6}	2.0906×10^{-6}
1660.0	3.4722×10^{-3}	0.2789	2.6688×10^{-6}	1.9769×10^{-6}	2.6688×10^{-6}
1860.0	3.4722×10^{-3}	0.2808	2.2875×10^{-6}	2.4352×10^{-6}	2.2875×10^{-6}
2060.0	3.4722×10^{-3}	0.2839	4.0500×10^{-6}	3.0000×10^{-6}	4.0500×10^{-6}
2260.0	3.4722×10^{-3}	0.2871	4.8125×10^{-6}	3.5648×10^{-6}	4.8125×10^{-6}
2460.0	3.4722×10^{-3}	0.2902	5.8344×10^{-6}	4.3218×10^{-6}	5.8344×10^{-6}
2660.0	3.4722×10^{-3}	0.2934	7.0093×10^{-6}	5.1921×10^{-6}	7.0093×10^{-6}
2860.0	3.4722×10^{-3}	0.2965	8.1437×10^{-6}	6.0324×10^{-6}	8.1437×10^{-6}
Cerachrome insulation; Pressure = 1.4700×10^{1} psia					
460.0	3.4722×10^{-3}	0.1648	6.7188×10^{-7}	4.9769×10^{-7}	6.7188×10^{-7}
660.0	3.4722×10^{-3}	0.1958	6.7188×10^{-7}	4.9769×10^{-7}	6.7188×10^{-7}
860.0	3.4722×10^{-3}	0.2268	1.0000×10^{-6}	7.4074×10^{-7}	1.0000×10^{-6}
1060.0	3.4722×10^{-3}	0.2482	1.3281×10^{-6}	9.8380×10^{-7}	1.3281×10^{-6}
1260.0	3.4722×10^{-3}	0.2640	1.6937×10^{-6}	1.2546×10^{-6}	1.6937×10^{-6}
1460.0	3.4722×10^{-3}	0.2726	2.1500×10^{-6}	1.5926×10^{-6}	2.1500×10^{-6}
1660.0	3.4722×10^{-3}	0.2789	2.7468×10^{-6}	2.0347×10^{-6}	2.7468×10^{-6}
1860.0	3.4722×10^{-3}	0.2808	3.3843×10^{-6}	2.5069×10^{-6}	3.3843×10^{-6}
2060.0	3.4722×10^{-3}	0.2839	4.1656×10^{-6}	3.0856×10^{-6}	4.1656×10^{-6}
2260.0	3.4722×10^{-3}	0.2871	4.9469×10^{-6}	3.6644×10^{-6}	4.9469×10^{-6}
2460.0	3.4722×10^{-3}	0.2902	5.9906×10^{-6}	4.4375×10^{-6}	5.9906×10^{-6}
2660.0	3.4722×10^{-3}	0.2934	7.1875×10^{-6}	5.3241×10^{-6}	7.1875×10^{-6}
2860.0	3.4722×10^{-3}	0.2965	8.3438×10^{-6}	6.1806×10^{-6}	8.3438×10^{-6}
RTV/Nomex felt					
460.0	0.0071	0.290	4.2100×10^{-7}	4.2100×10^{-7}	4.2100×10^{-7}
860.0	0.0071	0.290	5.2500×10^{-7}	5.2500×10^{-7}	5.2500×10^{-7}
1060.0	0.0071	0.290	8.8000×10^{-7}	8.8000×10^{-7}	8.8000×10^{-7}
2470.0	0.0071	0.290	1.7634×10^{-6}	1.7634×10^{-6}	1.7634×10^{-6}

Table V. Radiation Properties

Temperature, °R	Emissivity	Absorptivity	Reflectivity
Inconel 617 foil sheet			
520.0	0.85	0.85	0.15
2470.0	0.85	0.85	0.15
Blackbody			
520.0	1.00	1.00	0.00
2470.0	1.00	1.00	0.00

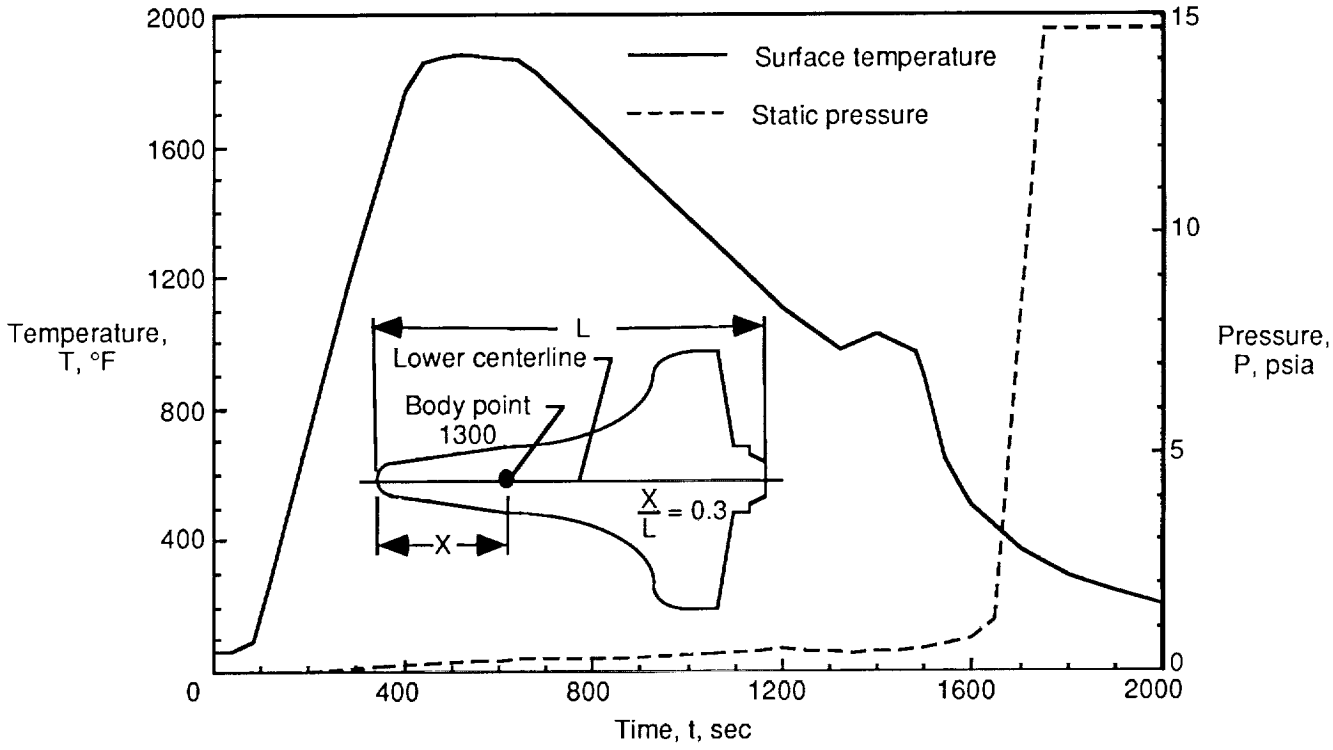

Figure 1. Entry surface temperature and static pressure histories. Shuttle body point 1300; trajectory 14414.1C.

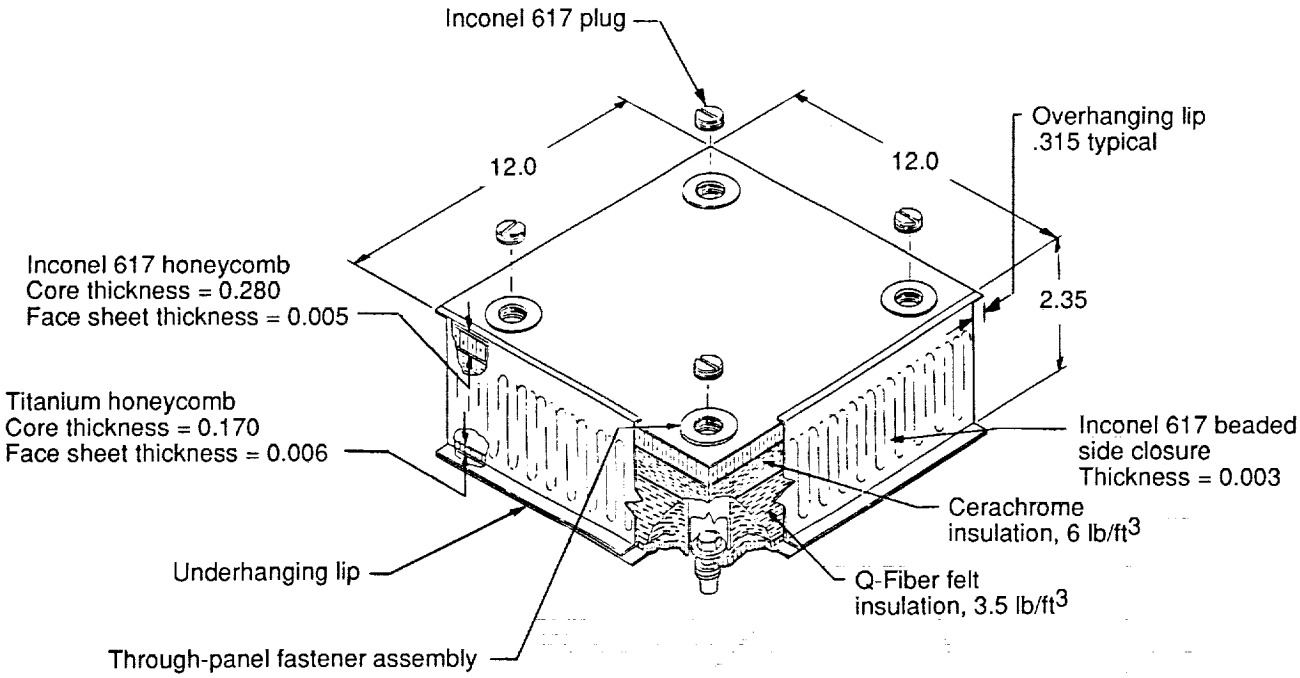

(a) Schematic.

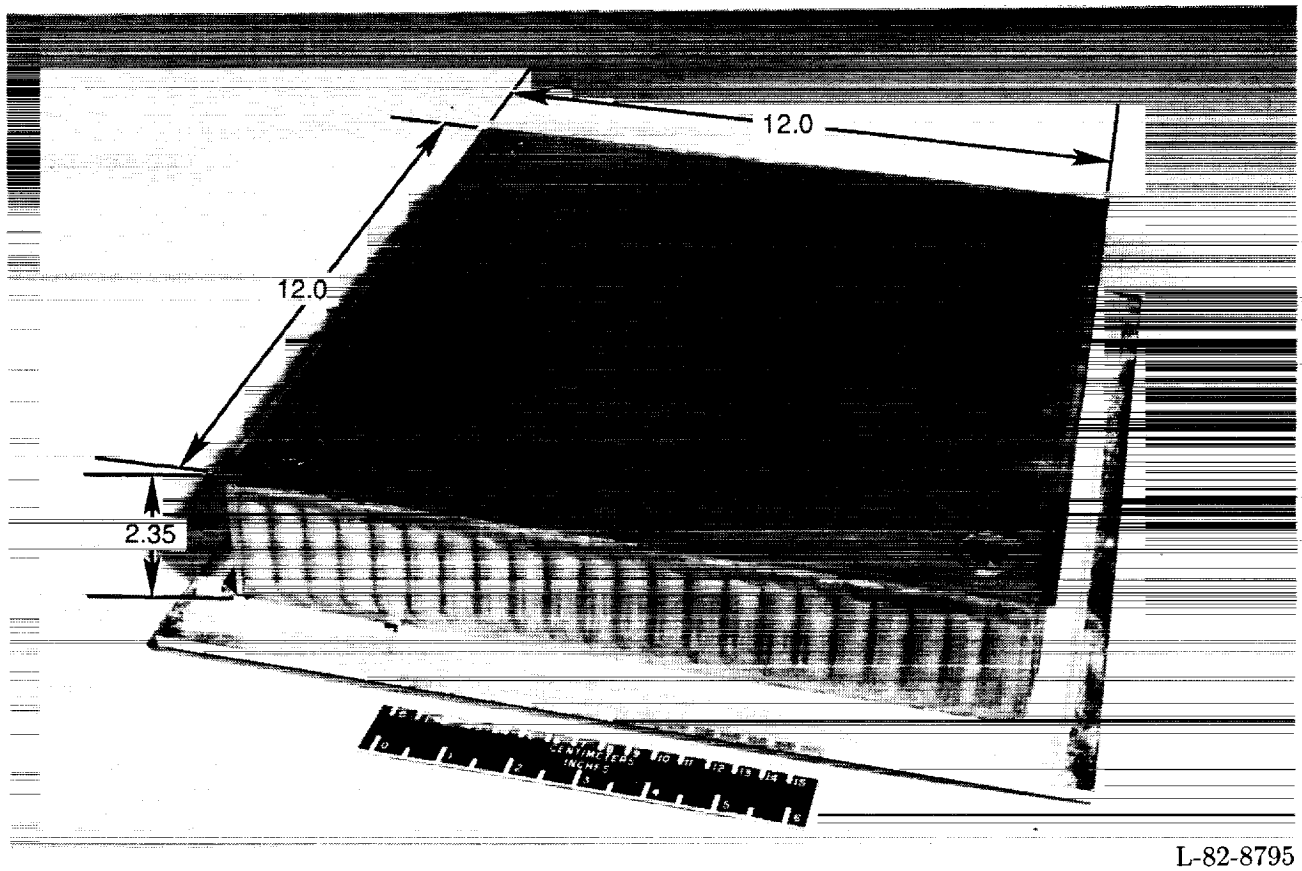

(b) Fabricated panel.

Figure 2. Superalloy honeycomb prepackaged thermal protection system panel. Dimensions are in inches unless otherwise noted.

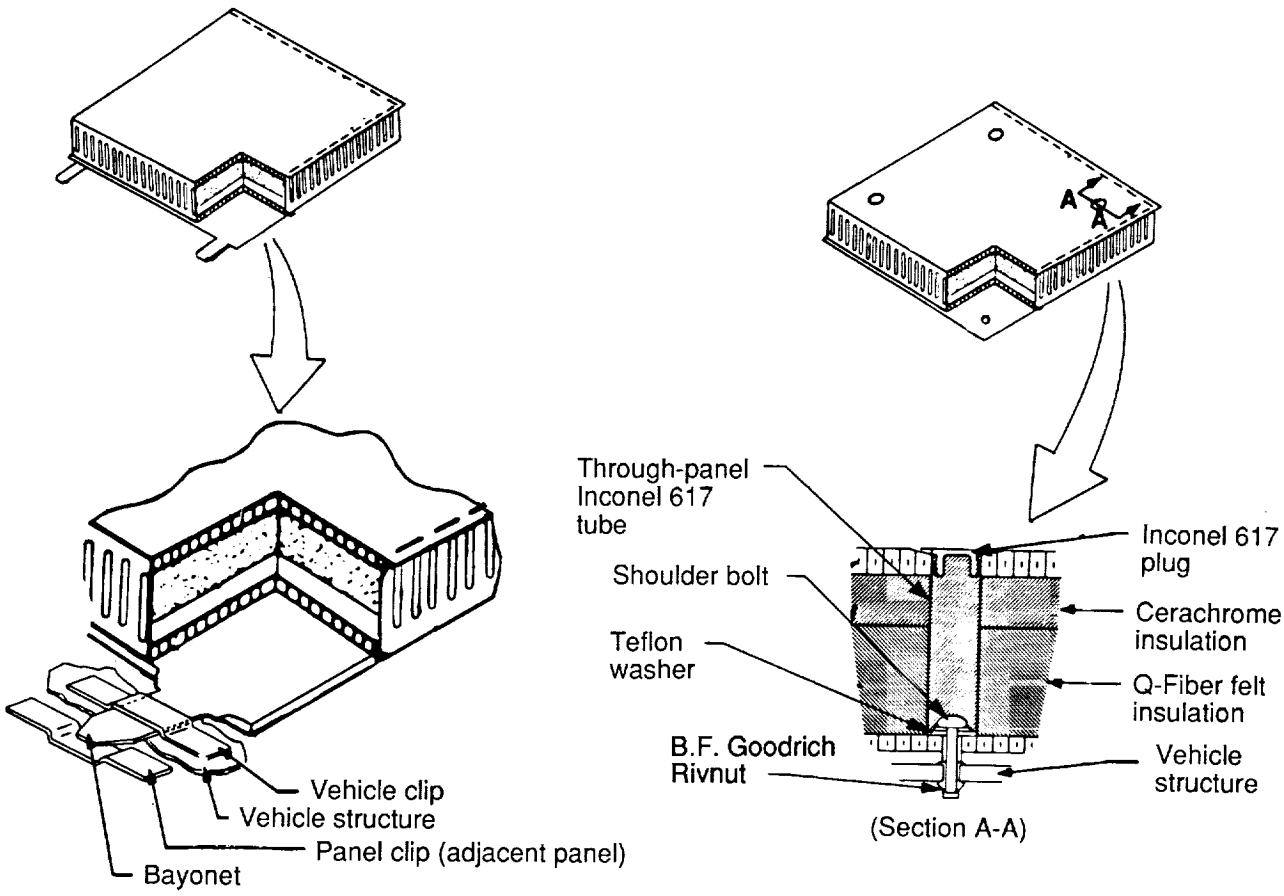

(a) Bayonet-clip attachment.

(b) Through-panel fastener.

Figure 3. Metallic thermal protection system attachment concepts.

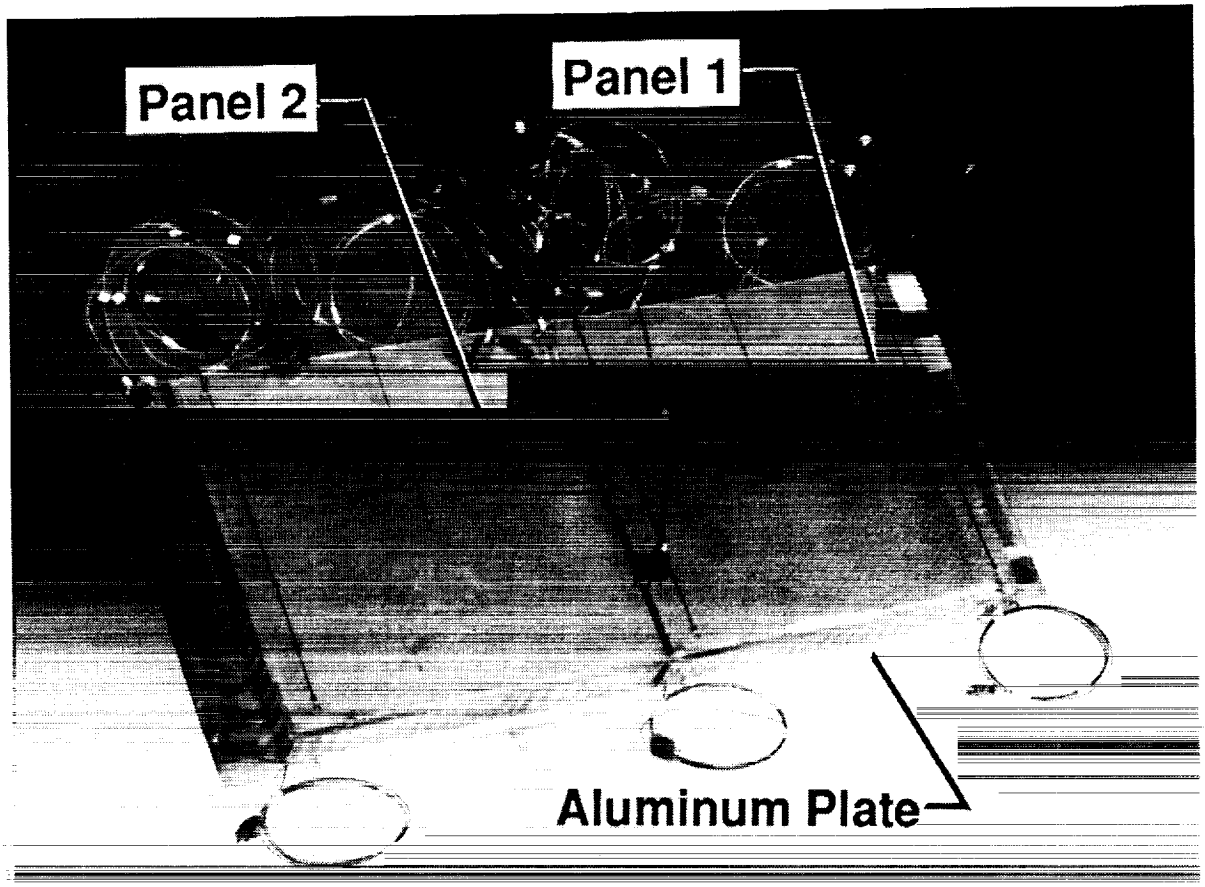

L-82-8801

Figure 4. Two-panel array before application of surface coating.

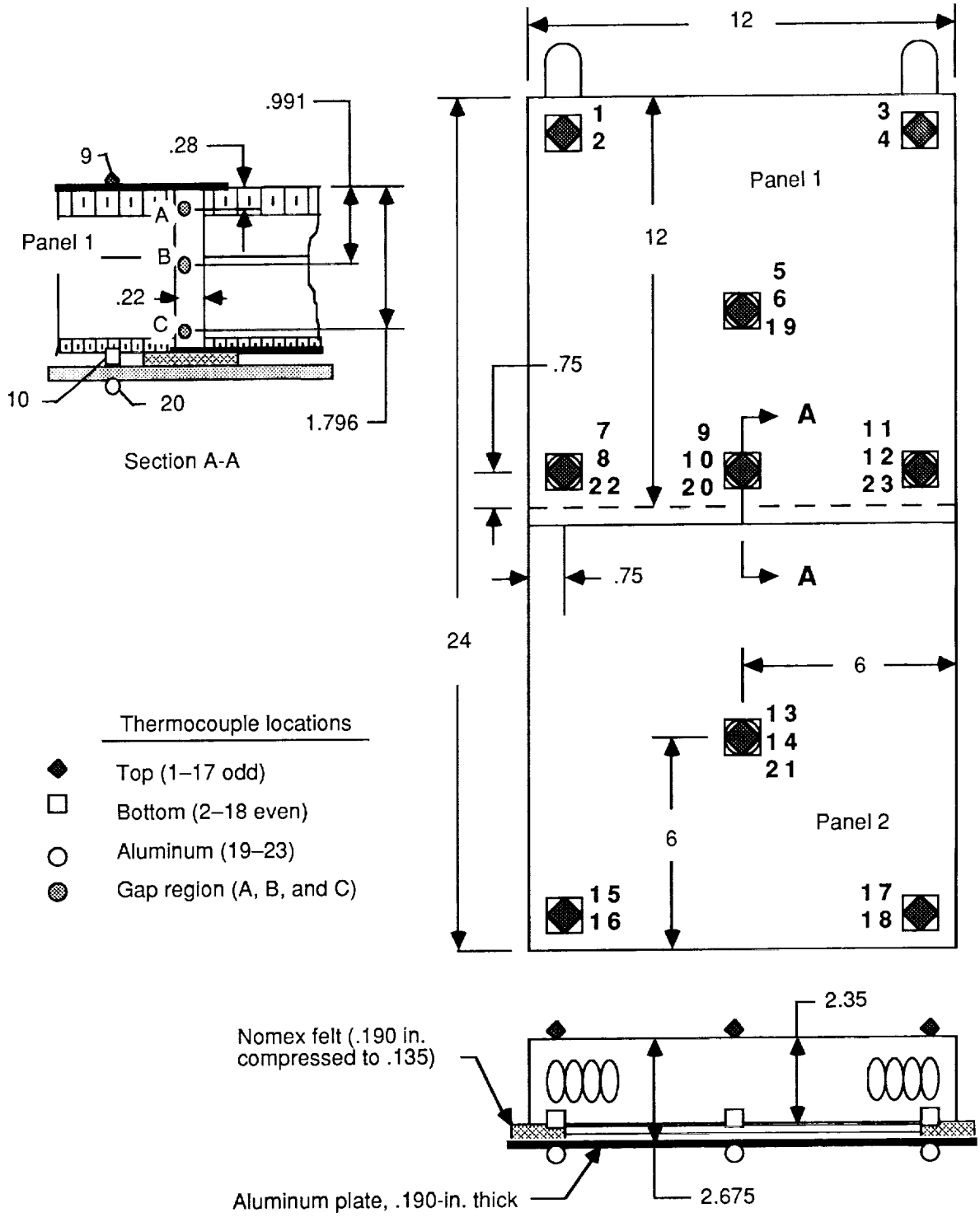

Figure 5. Thermocouple locations for two-panel array. Dimensions are in inches.

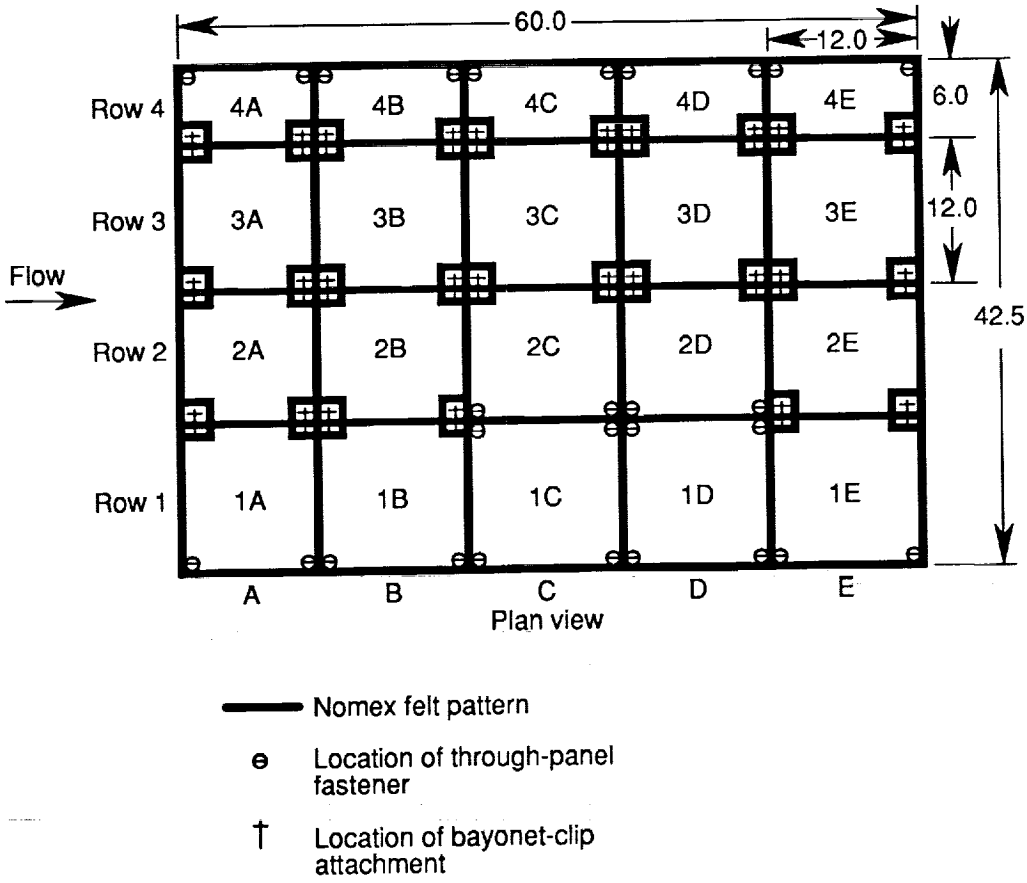

Figure 6. Locations of panels, fasteners, and Nomex felt used in the 20-panel array. Dimensions are in inches.

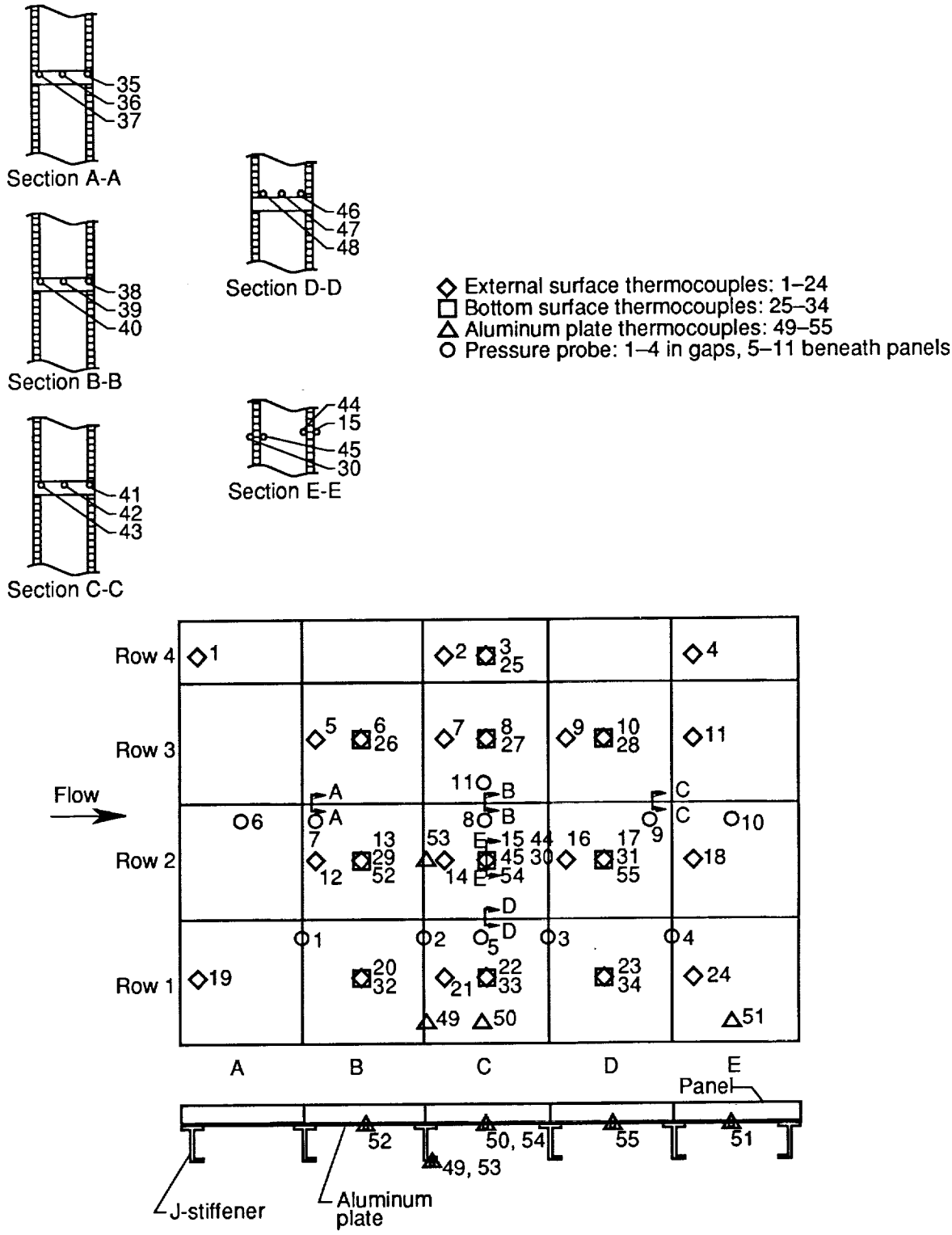

Figure 7. Thermocouple and pressure instrumentation locations for the 20-panel array.

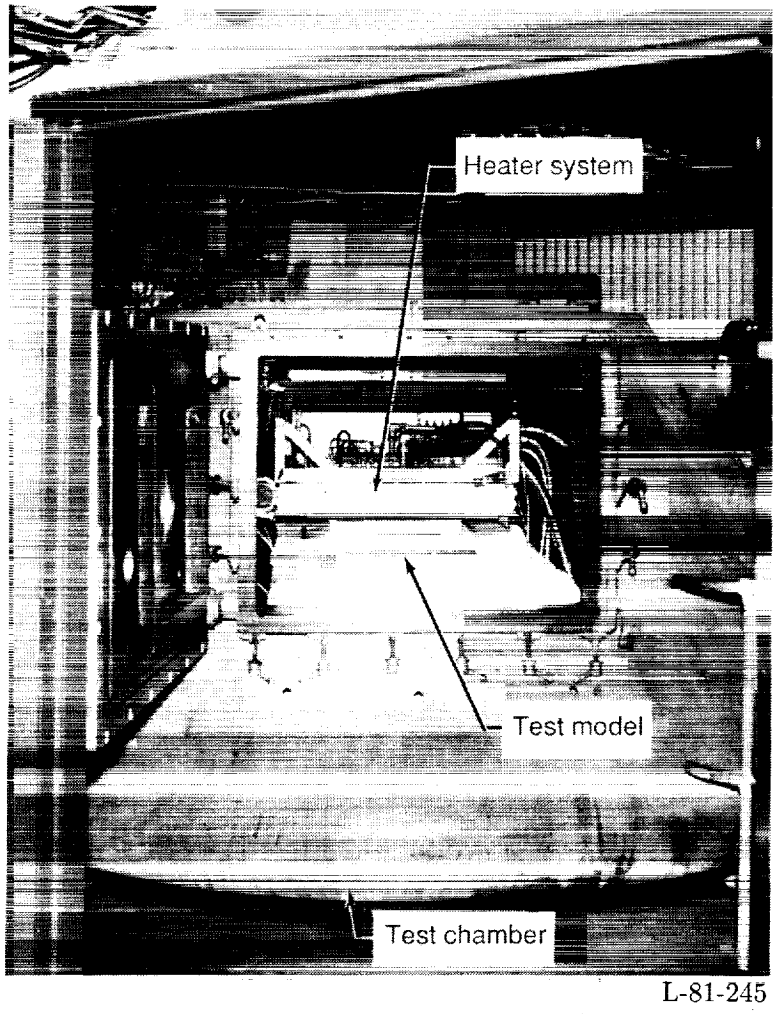

Figure 8. Radiant heating test chamber at Johnson Space Center.

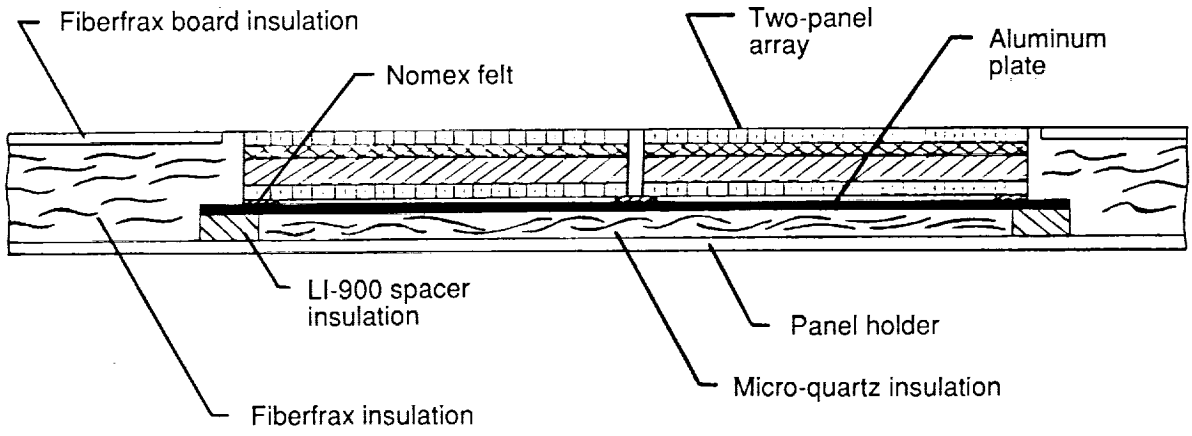

Figure 9. Section view of test model containing support structure and two-panel array.

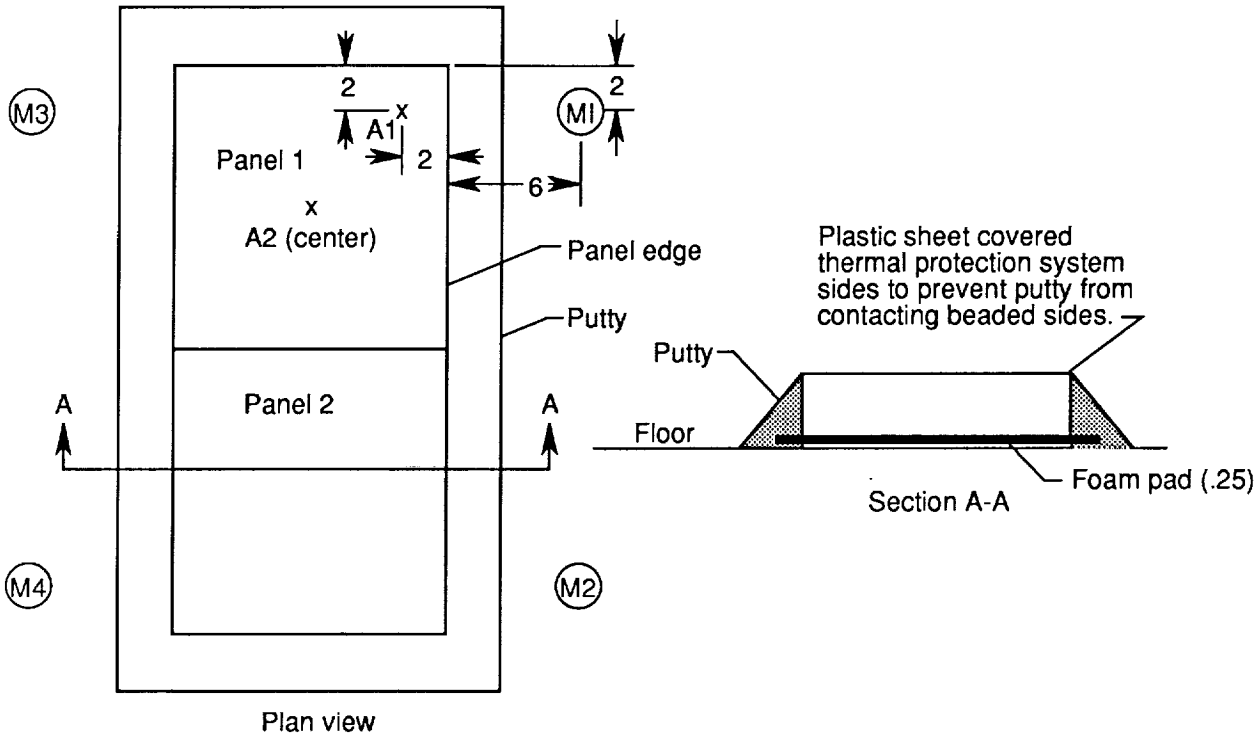

Figure 10. Metallic thermal protection system acoustic test assembly. M1–M4 are microphones; A1 and A2 are accelerometers; dimensions are in inches.

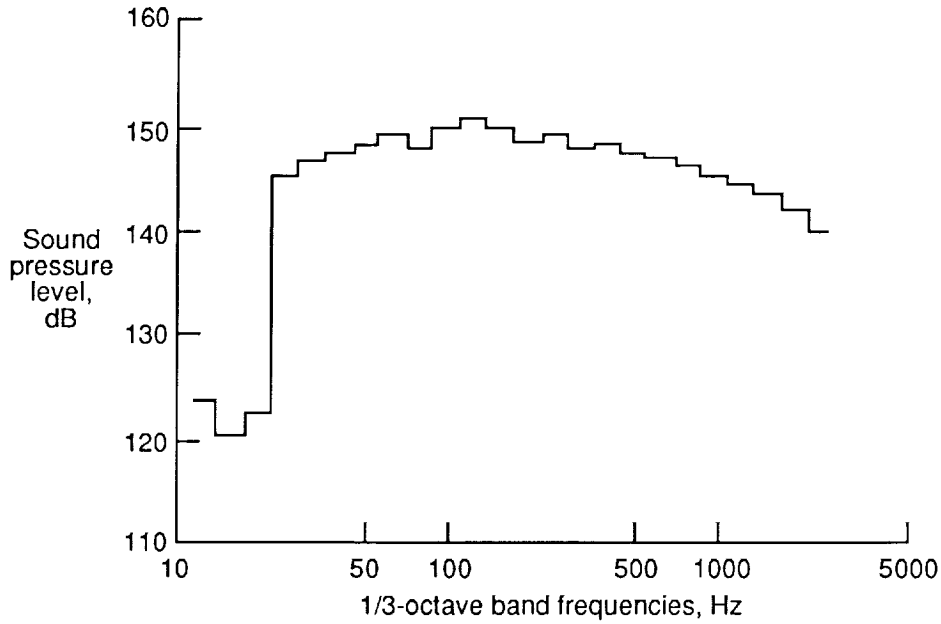

Figure 11. Acoustic spectrum for tests on two-panel array.

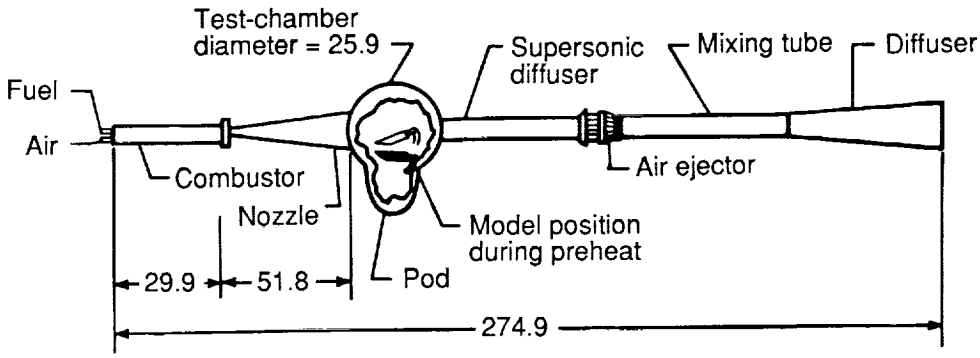

(a) Schematic of tunnel.

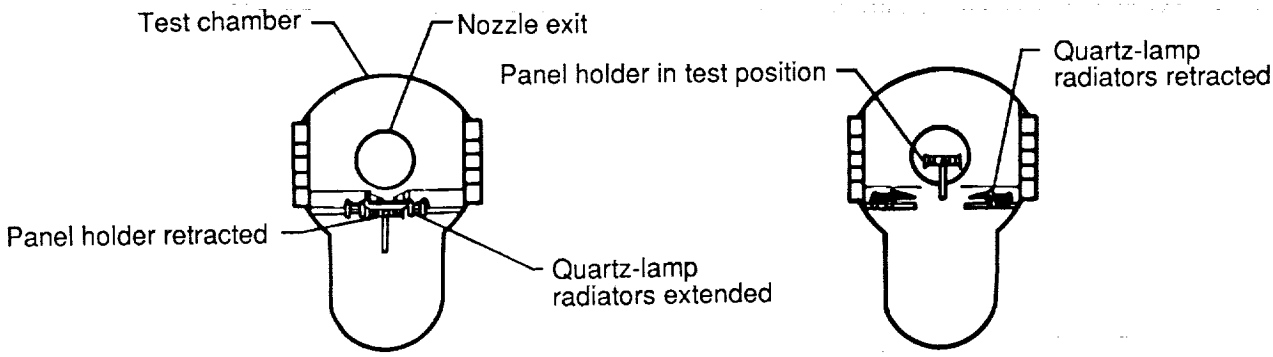

(b) Model position during preheat.

(c) Model position during test.

Figure 12. Schematic of Langley 8-Foot High-Temperature Tunnel. Dimensions are in feet.

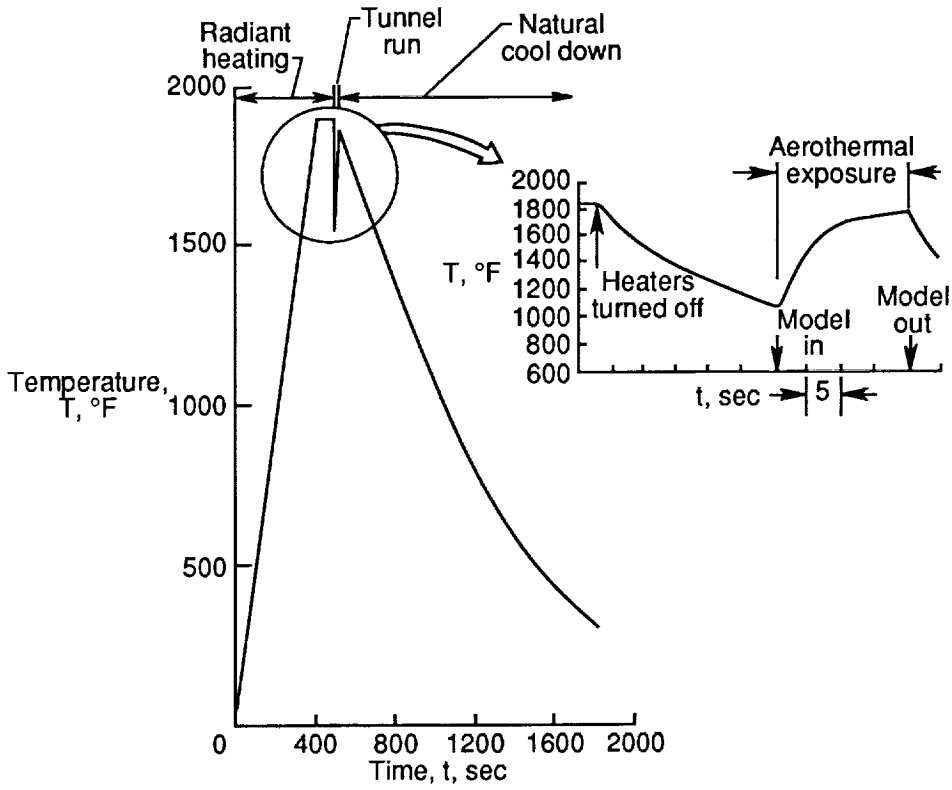

Figure 13. Typical temperature history of panel surface used in Langley 8-Foot High-Temperature Tunnel.

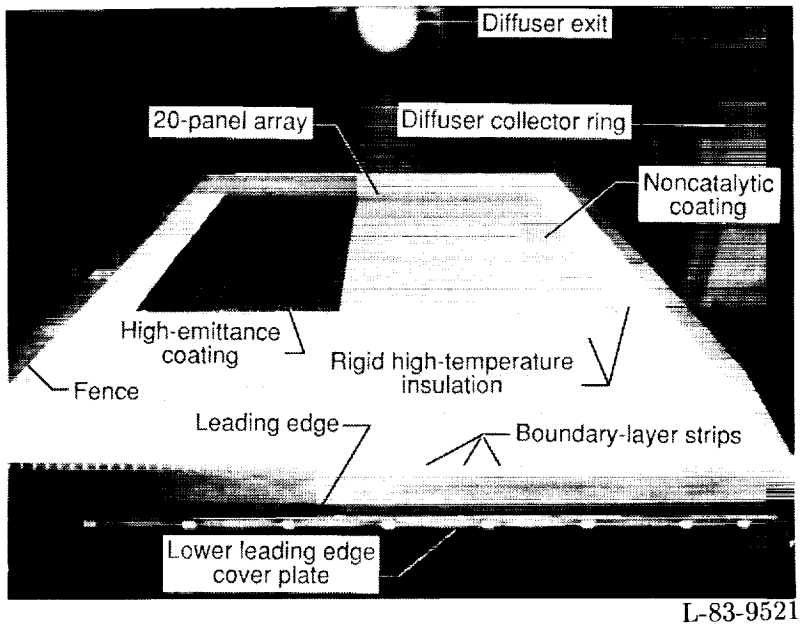

Figure 14. The 20-panel array and panel holder installed in the 8-Foot High-Temperature Tunnel.

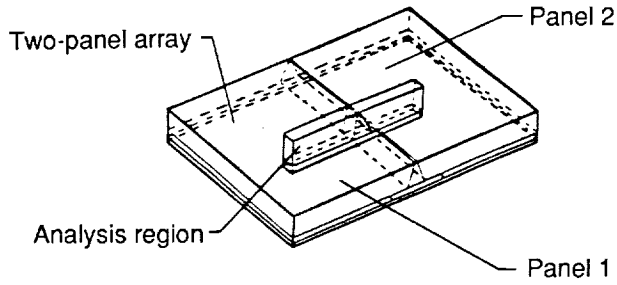

(a) Inconel 617 superalloy honeycomb two-panel array.

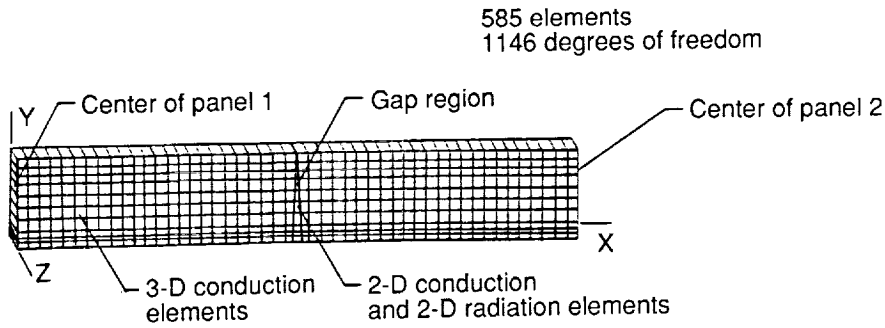

(b) Element grid.

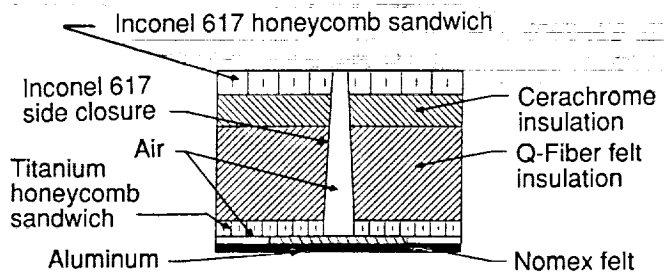

(c) Panel cross section.

Figure 15. Finite-element thermal model of two-panel array.

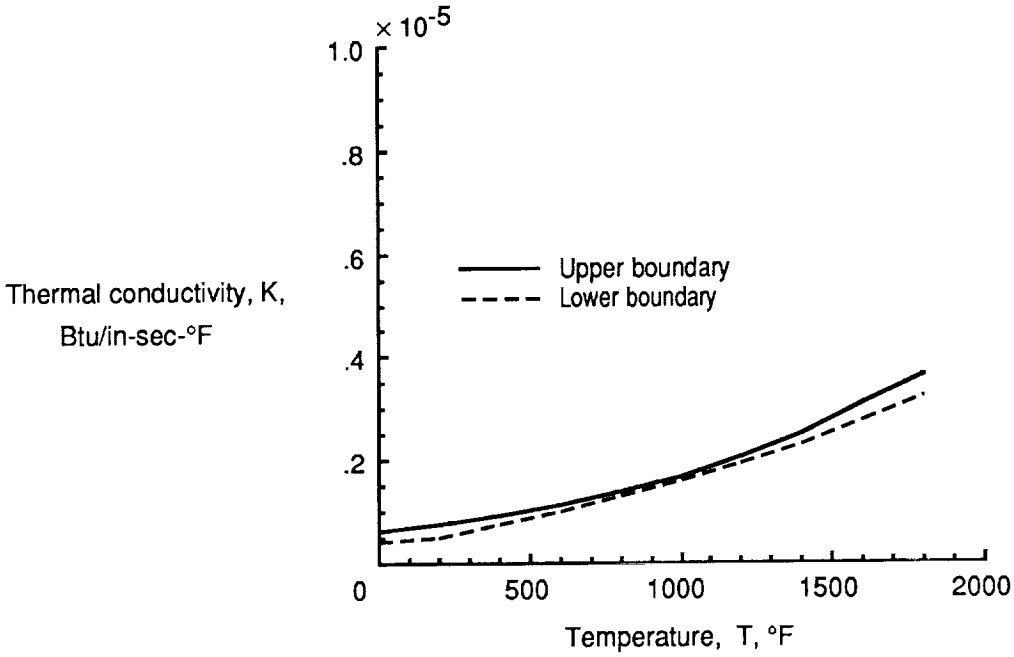

(a) Q-Fiber felt insulation. (Data from refs. 5 and 17–19.)

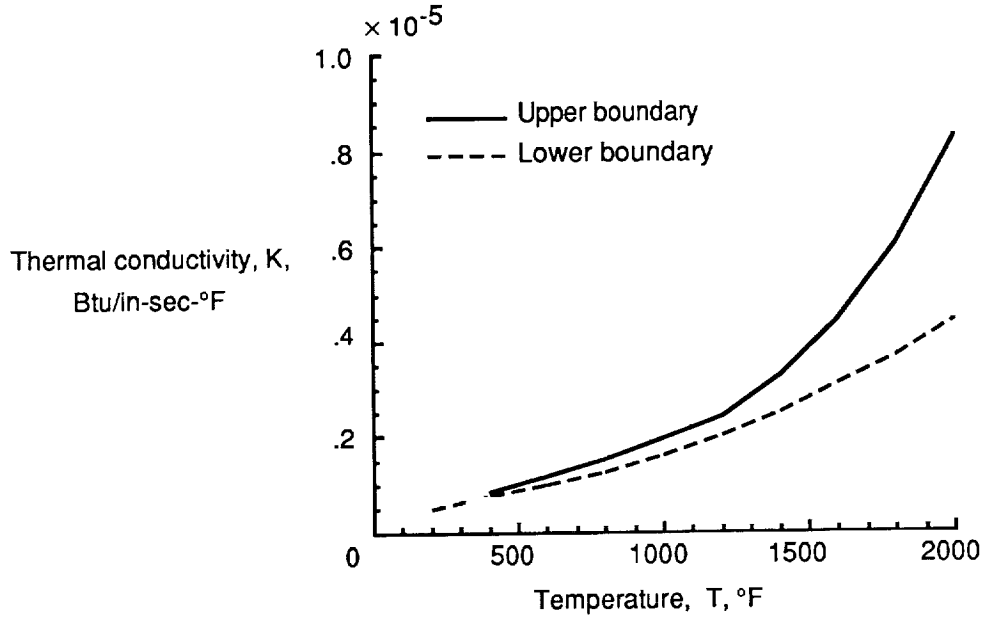

(b) Cerachrome insulation. (Data from refs. 5, 17, and 20.)

Figure 16. Effective thermal conductivity of insulation (through the thickness) at atmospheric pressure.

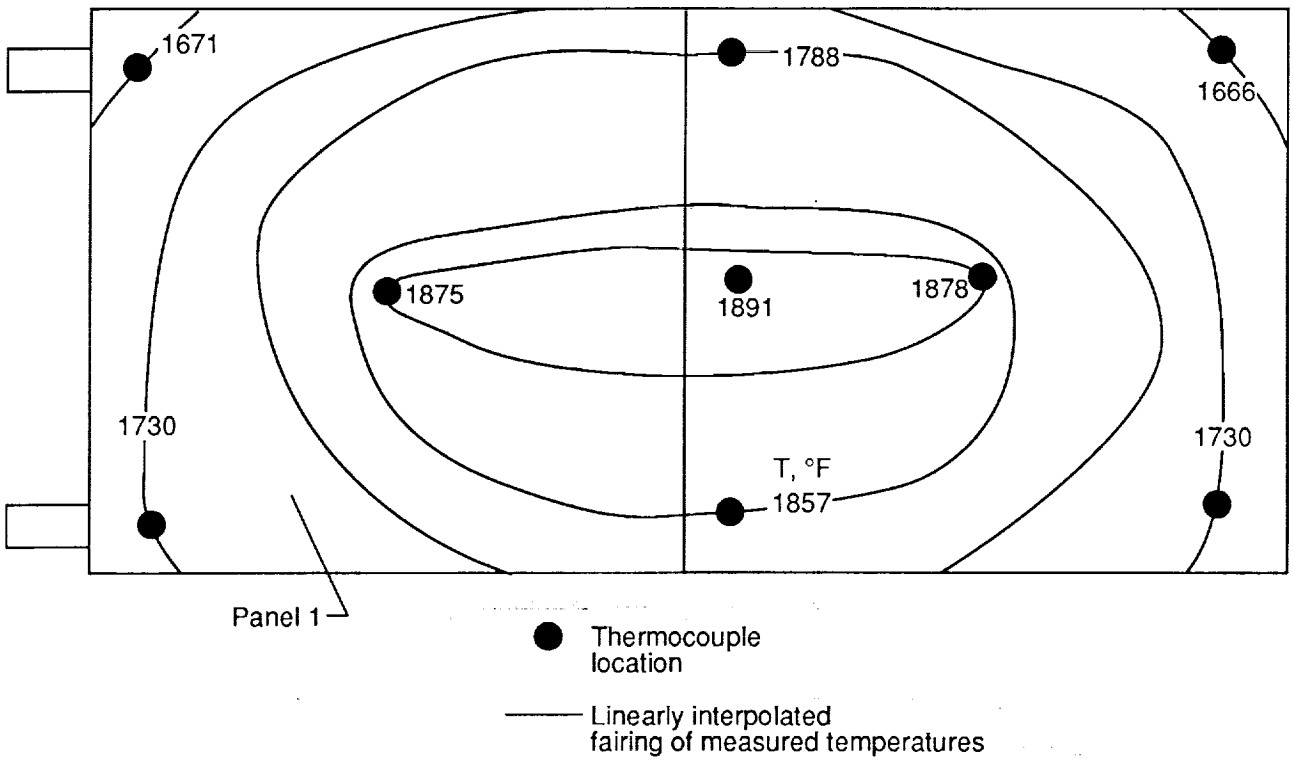

Figure 17. Surface temperature distribution of two-panel array; cycle 5, $t = 620$ sec.

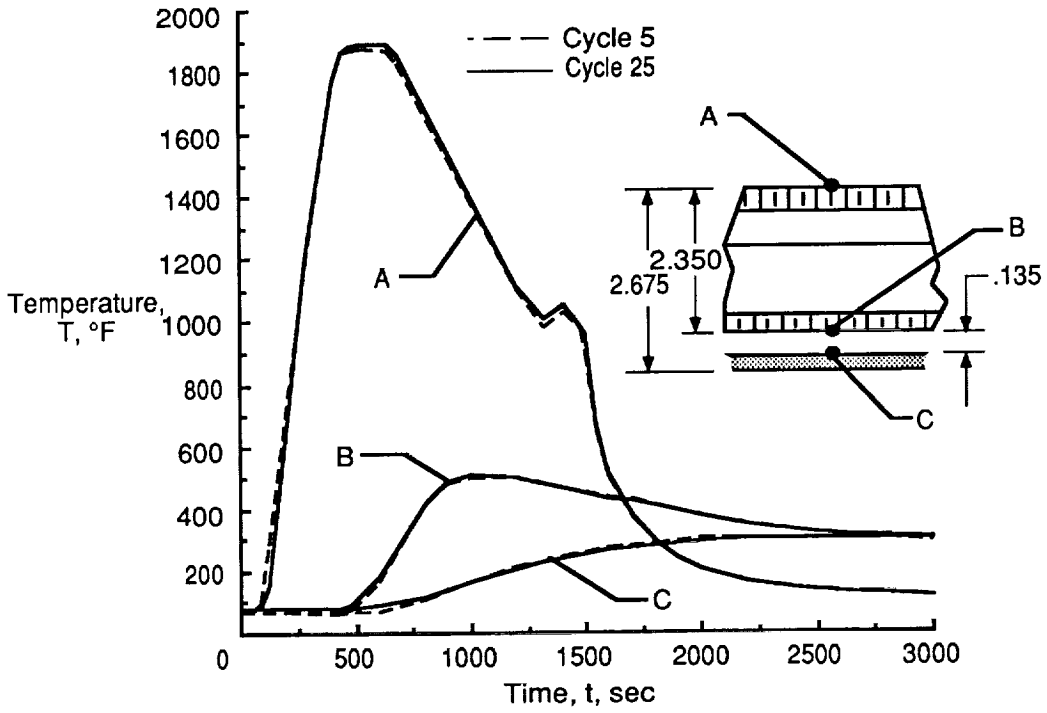

(a) Center of panel.

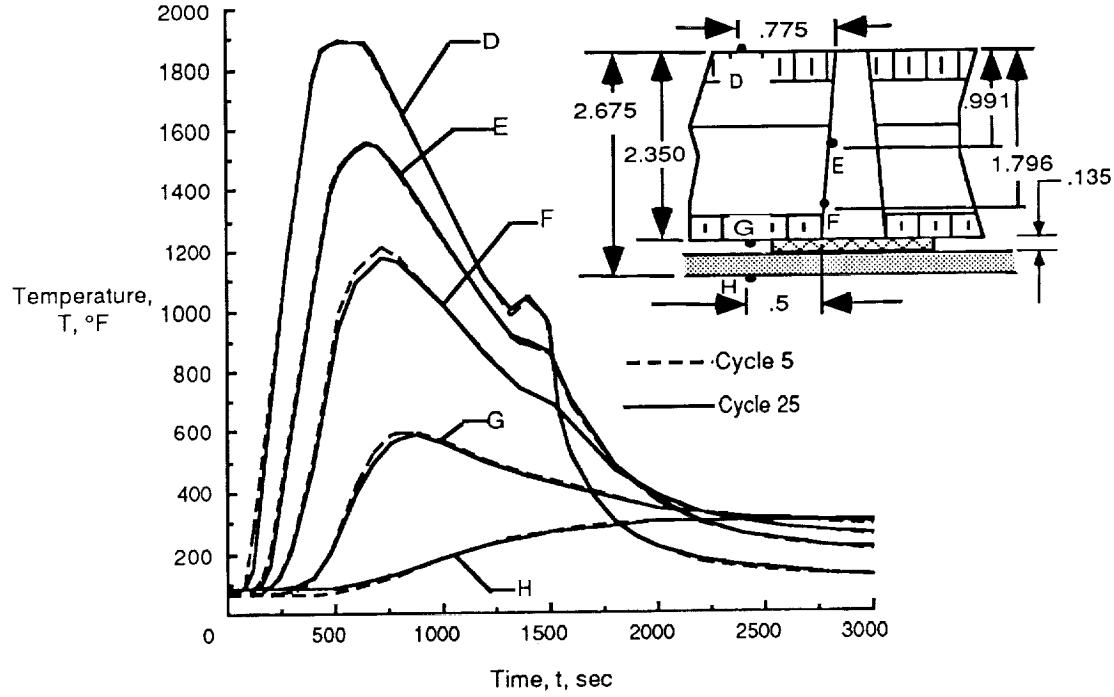

(b) Gap region.

Figure 18. Measured thermal performance of two-panel array. Dimensions are in inches.

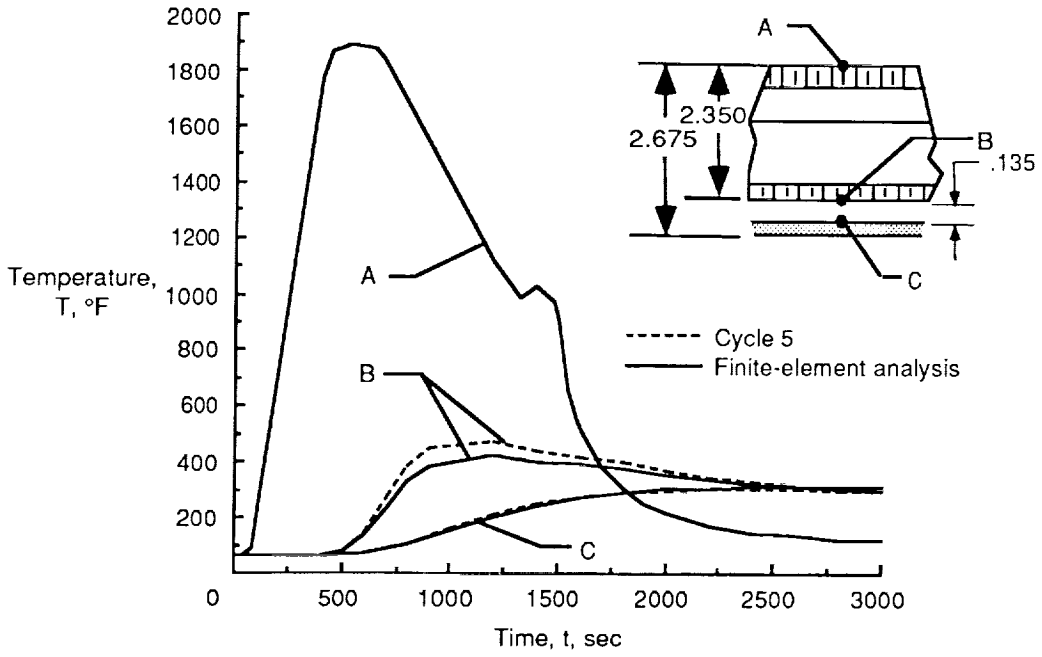

(a) Center of panel 1.

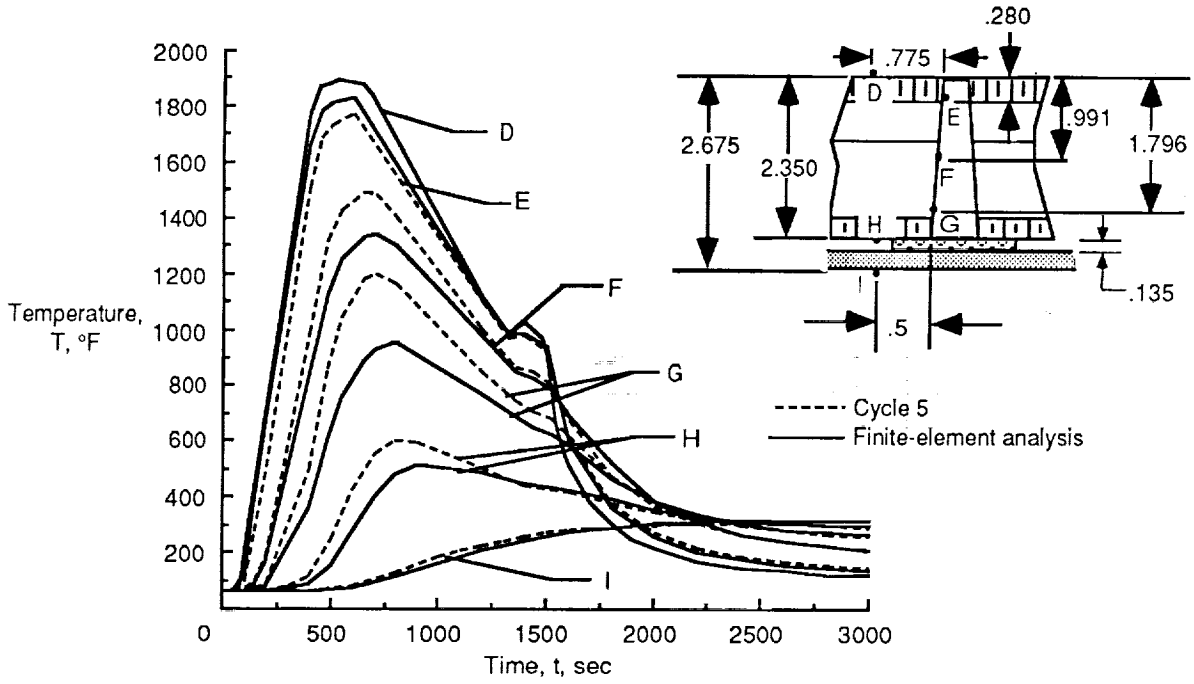

(b) Gap region.

Figure 19. Calculated and measured temperatures for two-panel array. Dimensions are in inches.

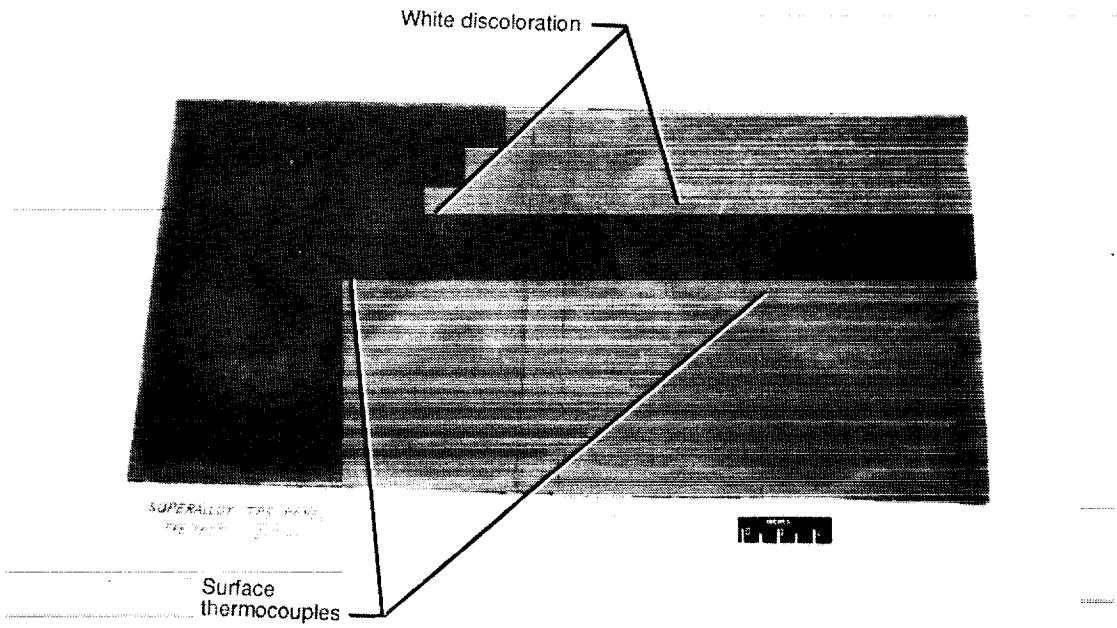

L-92-60

Figure 20. Two-panel array before testing.

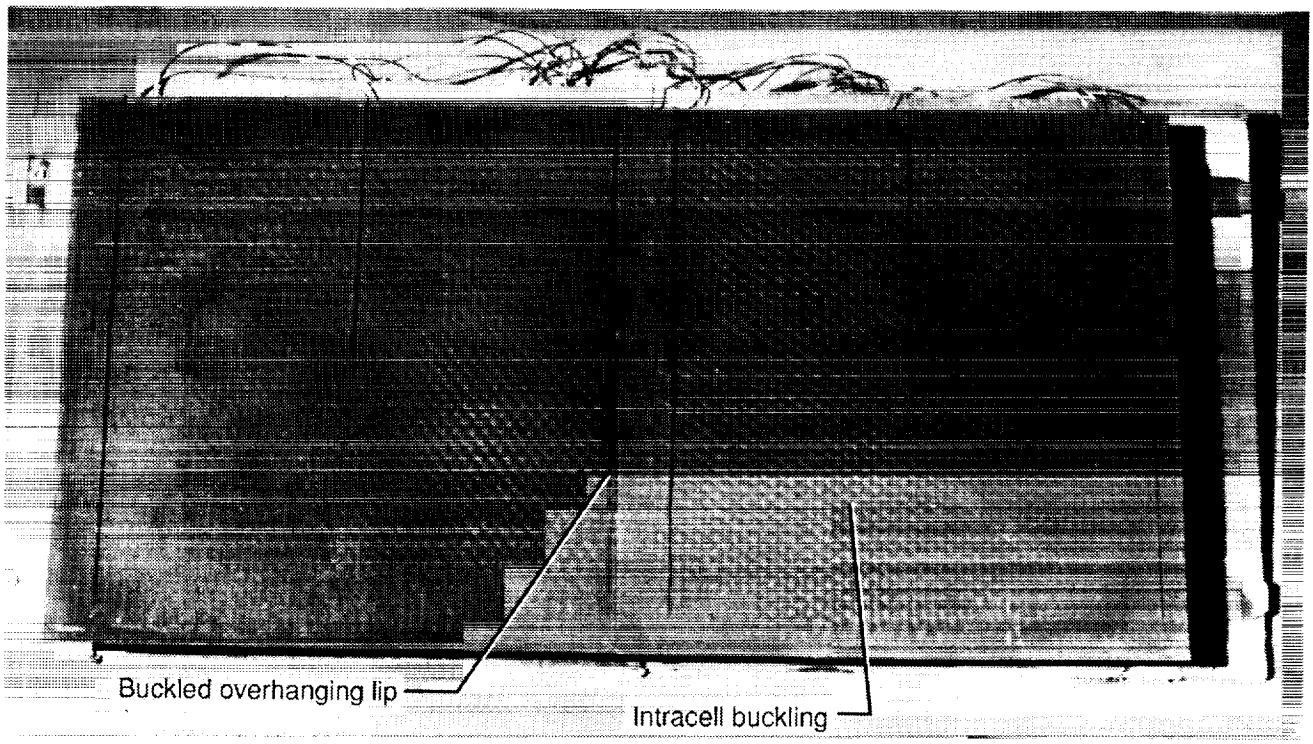

L-92-61

Figure 21. The 2-panel array after 26 thermal-pressure cycles.

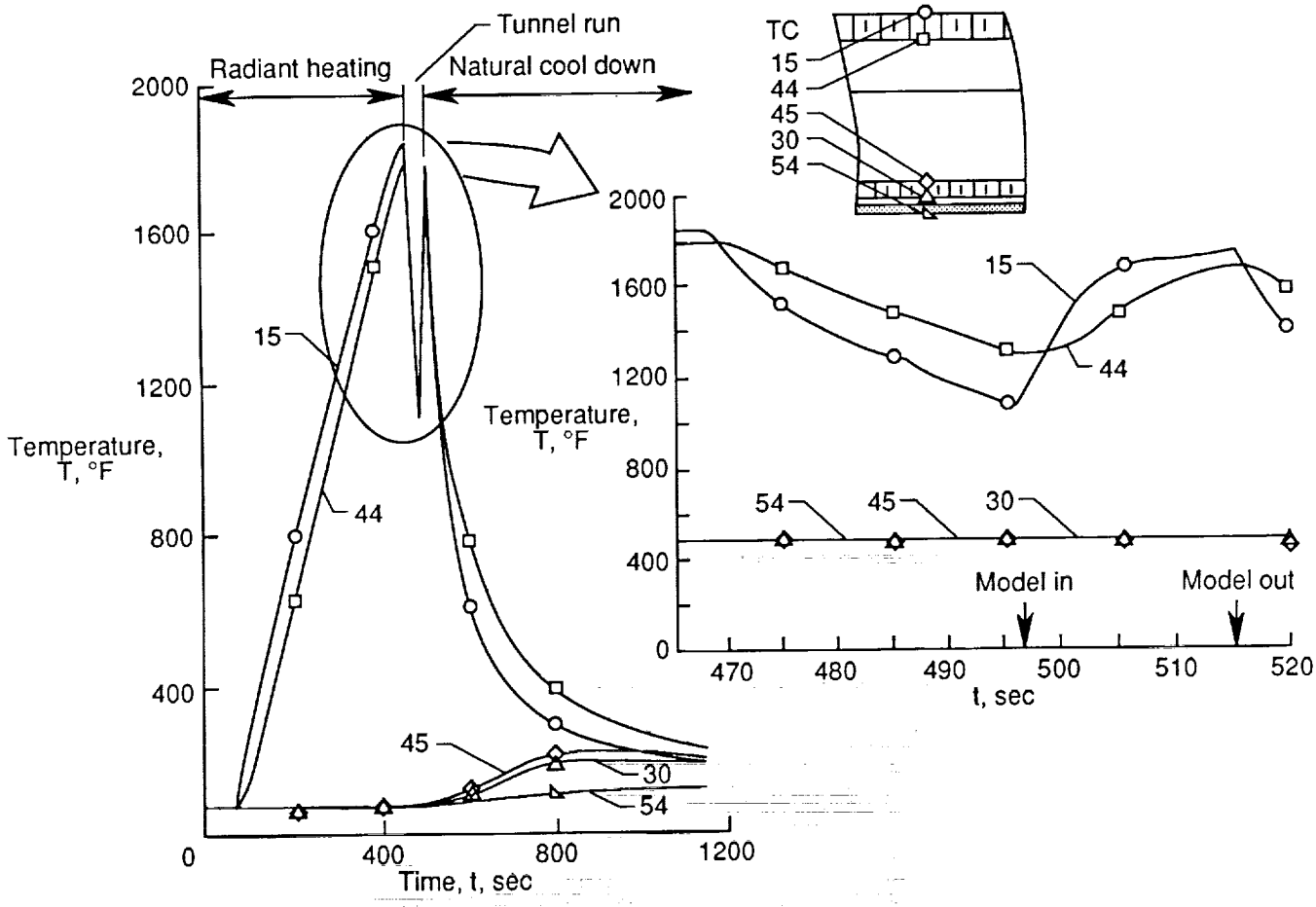

Figure 25. Temperature history at center of panel 2C of 20-panel array during test 13. TC indicates thermocouple.

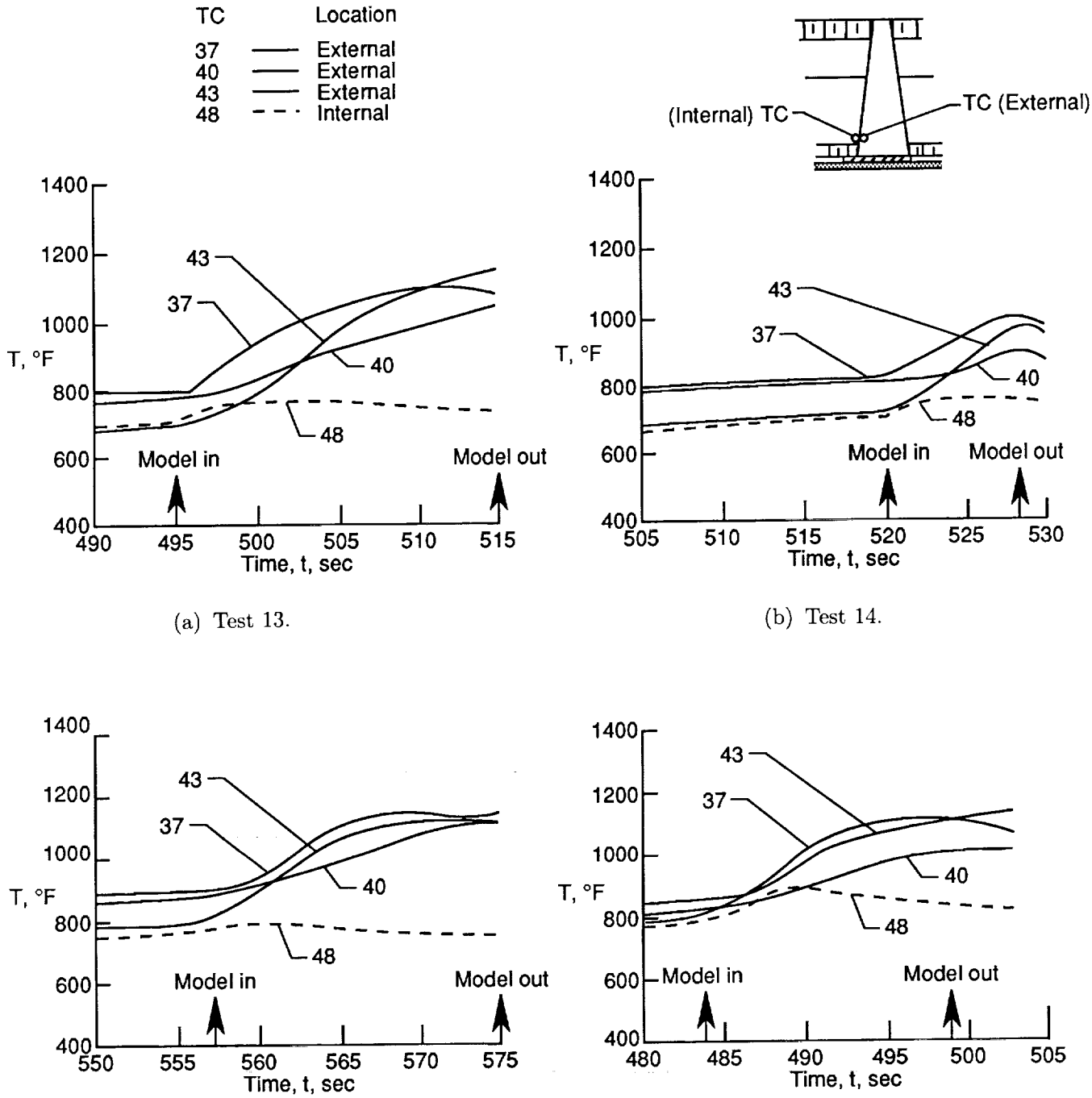

(a) Test 13.

(b) Test 14.

(c) Test 15.

(d) Test 20.

Figure 26. Temperature histories in gaps in 20-panel array. TC indicates thermocouple. (See fig. 7 for TC location.)

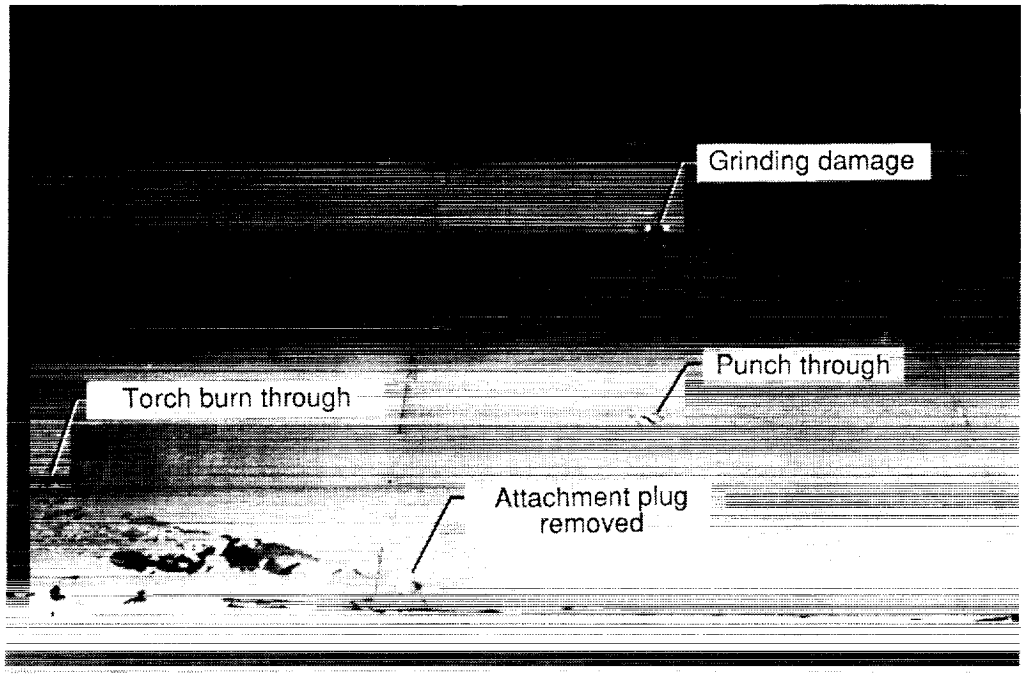

L-83-12449

Figure 27. Surface damage intentionally imposed on 20-panel array.

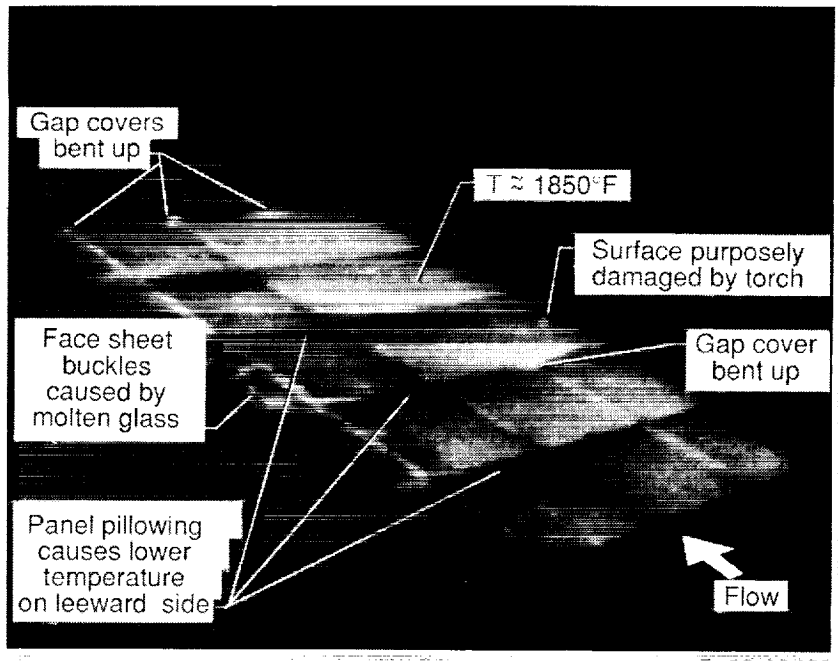

L-83-12439

Figure 28. The 20-panel array in the Langley 8-Foot High-Temperature Tunnel, test 20.

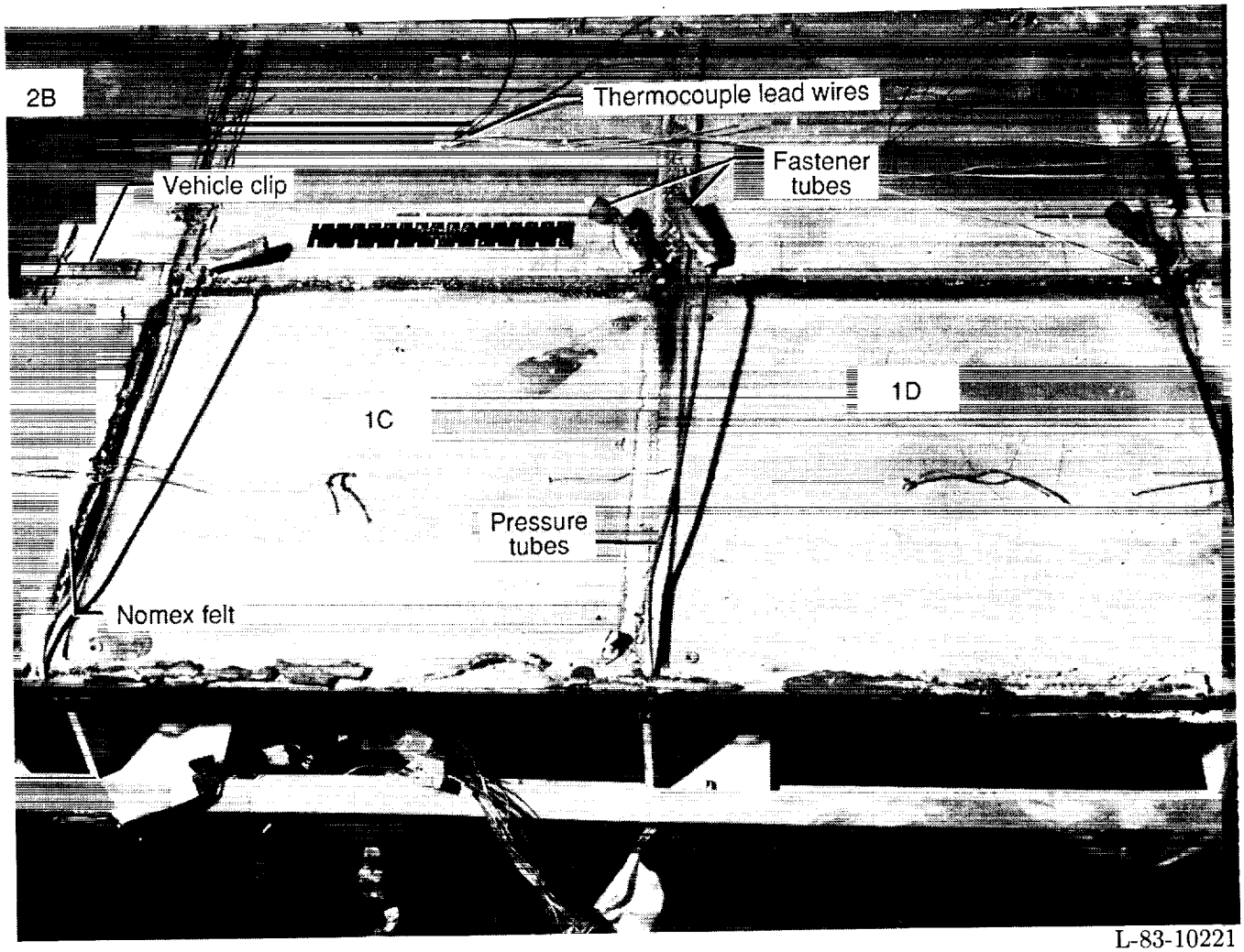

Figure 29. The 20-panel array after test 20.

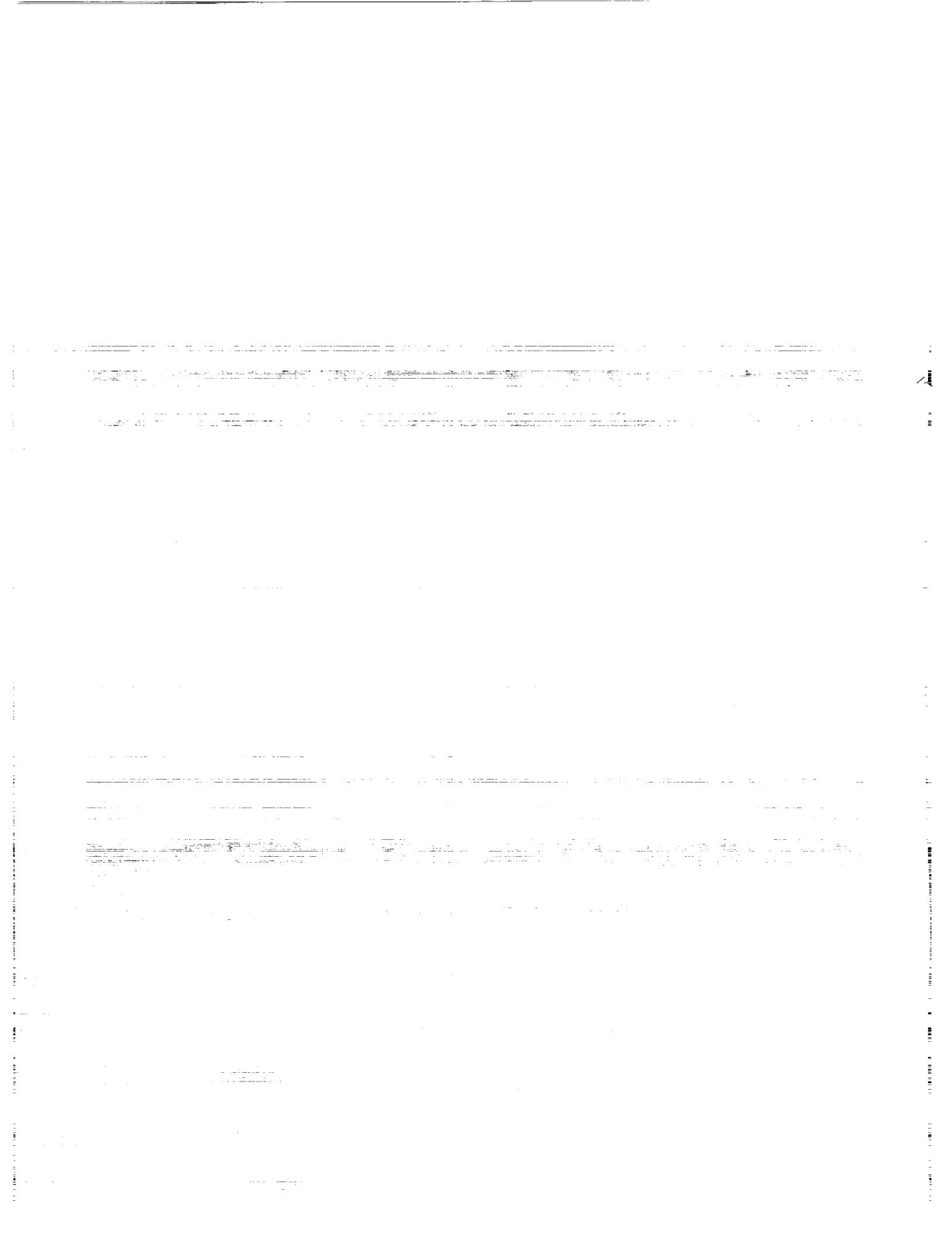

REPORT DOCUMENTATION PAGE

Form Approved
OMB No. 0704-0188

1. AGENCY USE ONLY *(Leave blank)*	2. REPORT DATE	3. REPORT TYPE AND DATES COVERED
	March 1993	Technical Paper

4. TITLE AND SUBTITLE
Static and Aerothermal Tests of a Superalloy Honeycomb Prepackaged Thermal Protection System

5. FUNDING NUMBERS
WU 506-43-71-04

6. AUTHOR(S)
Mark P. Gorton, John L. Shideler, and Granville L. Webb

7. PERFORMING ORGANIZATION NAME(S) AND ADDRESS(ES)
NASA Langley Research Center
Hampton, VA 23681-0001

8. PERFORMING ORGANIZATION REPORT NUMBER
L-17084

9. SPONSORING/MONITORING AGENCY NAME(S) AND ADDRESS(ES)
National Aeronautics and Space Administration
Washington, DC 20546-0001

10. SPONSORING/MONITORING AGENCY REPORT NUMBER
NASA TP-3257

11. SUPPLEMENTARY NOTES
Gorton: Lockheed Engineering & Sciences Company, Hampton, VA; Shideler and Webb: Langley Research Center, Hampton, VA.

12a. DISTRIBUTION/AVAILABILITY STATEMENT
Unclassified–Unlimited

Subject Category 34

12b. DISTRIBUTION CODE

13. ABSTRACT *(Maximum 200 words)*
A reusable metallic thermal protection system has been developed for vehicles with maximum surface temperatures of up to 2000°F. An array of two 12- by 12-in. panels was subjected to radiant heating tests that simulated Space Shuttle entry temperature and pressure histories. Results indicate that this thermal protection system, with a mass of 2.201 lbm/ft^2, can successfully prevent typical aluminum primary structure of an entry vehicle like the Space Shuttle from exceeding temperatures greater than 350°F at a location on the vehicle where the maximum surface temperature is 1900°F. A flat array of 20 panels was exposed to aerothermal flow conditions at a Mach number of 6.75. The panels were installed in a worst-case orientation with the gaps between panels parallel to the flow. Results from the aerothermal tests indicated that convective heating occurred from hot gas flow in the gaps between the panels. Proposed design changes to prevent gap heating include orienting panels so that gaps are not parallel to the flow and using a packaged, compressible *gap-filler* material between panels to block hot gas flow in the gaps.

14. SUBJECT TERMS
Thermal protection systems; Metallic prepackaged TPS; Radiant heating tests; High-temperature insulation

15. NUMBER OF PAGES
48

16. PRICE CODE
A03

17. SECURITY CLASSIFICATION OF REPORT	18. SECURITY CLASSIFICATION OF THIS PAGE	19. SECURITY CLASSIFICATION OF ABSTRACT	20. LIMITATION OF ABSTRACT
Unclassified	Unclassified		

NSN 7540-01-280-5500

Standard Form 298(Rev. 2-89)
Prescribed by ANSI Std. Z39-18
298-102

NASA-Langley, 1993